Available online at www.sciencedirect.com
SCIENCE DIRECT®
Polymer 45 (2004) 2665–2684
polymer
www.elsevier.com/locate/polymer

An experimental investigation of the large-strain tensile behavior of neat and rubber-toughened polycarbonate

E. Parsons, M.C. Boyce*, D.M. Parks

Department of Mechanical Engineering, Massachusetts Institute of Technology, Room 1-307, Cambridge, MA 02139, USA

Received 11 July 2003; received in revised form 15 January 2004; accepted 23 January 2004

Abstract

The large-strain tensile behavior of polycarbonate and polycarbonate filled with several volume fractions (f) of rubber particles is studied via an optical technique. Digital image correlation is used to determine, in two dimensions, the local displacement gradients and full-field displacements during a uniaxial tension test. Full-field strain contours, macroscopic true stress–strain behavior, and local volumetric strain are reduced from the raw test data. Full-field strain contours exhibit a decreasing degree of localization with increasing f. The true stress–strain results show a decrease in modulus, yield stress, post-yield strain softening, and subsequent strain hardening with increasing f. The volumetric strain decreases with increasing f as well. In the case of the neat polymer, comparisons are made to a three-dimensional finite element simulation.

Keywords: Rubber-toughened polymer; Tensile testing; Volumetric strain

1. Introduction

During a uniaxial tension test, most engineering polymers begin to deform inhomogeneously ('neck') at relatively small strains. Once necking begins, traditional extensometry techniques are rendered virtually useless. A contacting extensometer measures only the average strain over the gage length. Until the neck stabilizes and propagates the length of the specimen, however, the strain varies with axial position on the specimen. Any technique that seeks to determine the local true strain behavior must either use an infinitesimally small gage length or calculate the gradient in displacement in the axial direction. Furthermore, even in their neat form, most polymers exhibit a significant degree of dilatation during tensile extension. The deviation from incompressibility is attributed to crazing in glassy polymers and to crystal fragmentation in semi-crystalline polymers. In filled polymers, the debonding of rigid particulate fillers or the cavitation of elastomer fillers further weakens the assumption of incompressibility. The determination of the true stress at a given axial location on the specimen therefore requires knowledge of the lateral strains at that point. Strains must be measured not only in the axial direction but also in one (if transversely isotropic deformation may be assumed) or both lateral directions.

There have been numerous attempts to characterize the large-strain tensile behavior of polymers. The most successful endeavors used some type of video system to capture images of the specimen at various stages of extension. Buisson and Ravi-Chandar [1] applied a finely spaced grid to the surface of rectangular bar-type polycarbonate (PC) specimens. They calculated the axial and lateral displacement gradient at points along the specimen centerline by fitting polynomials to the grid line displacements. The true stress at the same points was obtained from a stress-optic method. In all of the studies described below, the true stress was calculated from the total load and the measured or assumed current cross-sectional area. Assuming incompressibility to obtain the axial strain, G'Sell et al. [2] calculated the true stress–strain behavior of several glassy and semi-crystalline polymers by using an optical diametral transducer to measure the instantaneous minimum diameter of hourglass-shaped cylindrical specimens. Nazarenko et al. [3] used a similar technique on round polycarbonate bars but applied a fine grid to the surface and also measured the behavior at points away from the site of neck initiation. Haynes and Coates [4] measured axial strain

* Corresponding author. Tel.: +1-617-253-2342; fax: +1-617-258-8742.
E-mail address: mcboyce@mit.edu (M.C. Boyce).

0032-3861/$ - see front matter © 2004 Elsevier Ltd. All rights reserved.
doi:10.1016/j.polymer.2004.01.068

as a function of axial position in polypropylene and a styrene butadiene elastomer by tracking the axial position of transverse grid lines printed on the surface of rectangular bar-type specimens. The true axial strain was taken directly from the relative displacement between neighboring grid lines, and the true axial stress was then calculated by assuming constant volume deformation. Gloaguen and Lefebvre [5] calculated the true stress–strain and volumetric strain behavior of nylon and polypropylene by measuring the separation of pairs of ink marks on rectangular bar-type specimens. Two cameras were used to measure simultaneously the strains in all three directions. Homogeneous deformation between the ink marks was assumed. G'Sell et al. [6] later developed an optical technique for use on rectangular bar-type specimens which did not require the assumption of constant volume and also allowed for a degree of inhomogeneous axial deformation. The locations of seven dots on the surface of the specimen were used to calculate the true axial and lateral strains at a particular axial location. Assuming a transversely isotropic strain tensor, they calculated the true stress–strain and volumetric strain behavior of polyethylene terephthalate and high-impact polystyrene.

The experimental technique utilized in this study, digital image correlation (DIC), has advantages over all of the previously described techniques. DIC is simply the process of matching subsets of pixel gray-value patterns from one image to another. When DIC is applied to a mechanical test, an image of the deformed specimen is correlated to an image of the undeformed specimen, and the in-plane displacements and the displacement gradient are calculated for one or more pixel subsets. From the displacement field or the displacement gradient, any type of strain measure may be calculated. With all in-plane strain components known, the assumption of incompressibility made by several afore-mentioned authors is not necessary. A procedure will be introduced which enables measurement of the strain in the third dimension as well. The strain calculation allows for large strain gradients and, hence, works well on materials that deform inhomogeneously. Furthermore, by performing the analysis on numerous subsets, one can construct full-field contours of strain and examine behavior as a function of position.

Laraba-Abbes et al. [7] used DIC to measure the nominal stress-stretch behavior of carbon black-filled natural rubber. During a tension test, they illuminated the rectangular bar-type specimen surface with a laser and captured images of the reflected light with a charged couple device (CCD) camera. Due to the imperfection of the specimen surface, the reflected light exhibited a spatial variation in intensity or 'speckle' effect. Forming a digital signature of the specimen surface, the distribution of light detected at the camera sensor is what is known as a 'speckle pattern'. Starting with the undeformed image, Laraba-Abbes et al. incrementally obtained the in-plane displacement field by correlating subsets of the speckle pattern from one image to the next. They calculated the in-plane axial and transverse stretches by differentiating linear functions fit to subsets of the displacement field.

In this study, the DIC method is used to measure, in two dimensions, the local displacement gradient and the full-field displacements during a standard uniaxial tension test. A random speckle pattern is applied with ink to the surface of rectangular bar-type PC specimens. A CCD camera connected to a computer acquires digitized images of the specimen surface at regular intervals during a tensile test. The in-plane displacement gradient and displacements are calculated in the Lagrangian description by correlating subsets in the undeformed (reference) image to subsets in each deformed image. From the raw displacement data, true stress–strain and volumetric strain behavior and full-field strain contours are constructed.

The outline of the paper is as follows: in Section 2, the procedure is described. The experimental technique and DIC algorithm is briefly discussed, and the method for calculating the large-strain measure and the true stress from the raw correlation (displacement) data and macroscopic load is then given. The finite element model of the neat PC uniaxial tension test is described as well. In Section 3, the experimental results are presented, and, at the same time, the algorithms for determining the true stress–strain and volumetric strain behavior are developed and validated by drawing comparison to the results of the finite element simulation. In order to illustrate the general features of polymer deformation, the section begins with full-field contours of strain for neat PC and compares the experimental results to the simulation results. Next, in Section 3.2, the local axial and lateral strains in neat PC are investigated as a function of time and position on the tensile specimen. Finding that the strains are a strong function of lateral position, we define macroscopic quantities to represent the true axial and lateral strains. In Section 3.3, the spatial variation of the true stress–strain and axial strain rate history is investigated on the neat PC specimen. Data reduction schemes are developed to extract the material true stress–strain behavior from the raw specimen data. The simulation emulates the experimental conditions and verifies the efficacy of the data reduction strategies. Similarly, in Section 3.4, the simulation indicates how most accurately to calculate the volumetric strain in neat PC. Finally, in Section 3.5, the true stress–strain, volumetric strain and full-field strain results for rubber-filled PC at three different volume fractions of modifier are presented and discussed. The paper concludes with a short discussion in Section 4.

2. Procedure

2.1. Sample preparation

The material used in this study was a polycarbonate,

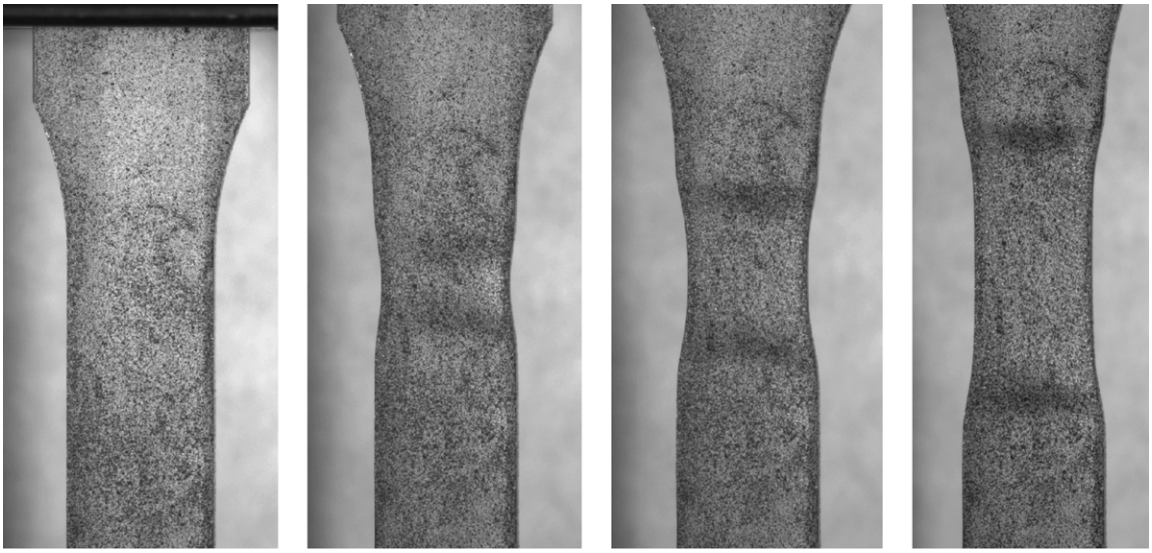

Fig. 1. Front view images of a neat PC tensile bar: (a) reference image, (b)–(d) deformed images.

trade name Makrolon 2608, supplied by Bayer Corporation (Pittsburgh, PA). The homopolymer and blends containing, by volume, 5%, 15%, and 25% core-shell rubber particles were tested. The particles, supplied by Rohm and Hass, had a methyl-methacrylate/styrene shell and a polybutadiene core. Johnson [8] reported the particle diameters to range from 0.3 μm to 0.8 μm with a mean of 0.52 μm. The neat polymer and blends were injection molded into 12.7 mm × 12.7 mm × 127 mm bars. Tensile bars with gage section dimensions 19.05 mm × 7.62 mm × 3.20 mm were machined from the square bars.

2.2. Testing procedure

All tensile tests were conducted on an Instron model 5582 screw machine at a constant nominal strain rate of 0.005 s^{-1}. A random speckle pattern was applied to each specimen with either a Sanford sharp tip marker or a Badger airbrush filled with India ink. The pattern density was maximized under the constraint that individual speckles should generally not overlap. The minimum characteristic speckle size was three pixels. High resolution (1280 pixels × 1024 pixels), 12-bit images were recorded at a frequency of 1 Hz with a Qimaging Retiga 1300 CCD camera equipped with a 200 mm Canon f/4.0 Canon lens and, in some cases, a Nikon 200 mm extension. The camera was placed at a distance of 1.0 m from the specimen. Fig. 1 shows four images captured without the lens extension. The load at the time of each image acquisition was recorded via a National Instruments DAQ board. It was not assumed that the specimens would deform isotropically in the two lateral directions. Therefore, as illustrated in Fig. 2, companion tests were viewed from two orientations; the 'front' view captured the deformation of the thick lateral dimension (x), and the 'side' view captured the deformation of the thin lateral dimension (z).

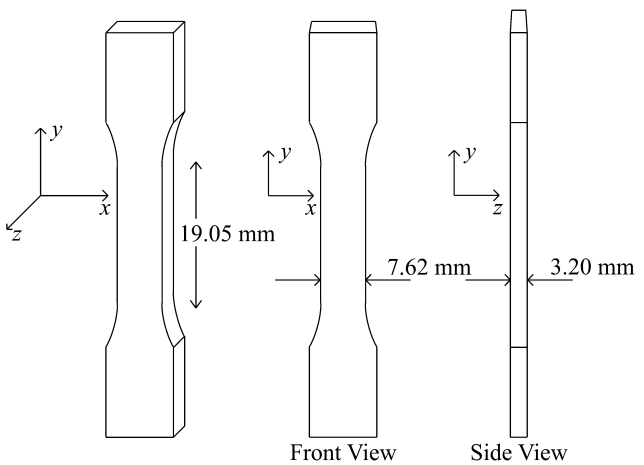

Fig. 2. Specimen geometry and definition of views and coordinate directions.

2.3. Strain measurement

The images were analyzed with a DIC algorithm developed and implemented by Correlated Solutions Incorporated (CSI)[1]. To correlate the deformed image to the reference image, the area of interest in each image is divided into small square subsets. The discrete matrix of the pixel gray level values in each subset forms a unique pattern

[1] West Columbia, SC 29169, USA. Tel.: +1-803-926-7272; url: www.correlatedsolutions.com.

within the image. The second-order shape functions

$$u(x,y) = u_c + \frac{\partial u}{\partial x}(x - x_c) + \frac{\partial u}{\partial y}(y - y_c) + \frac{1}{2}\frac{\partial^2 u}{\partial x^2}(x - x_c)^2 + \frac{\partial^2 u}{\partial x \partial y}(x - x_c)(y - y_c) + \frac{1}{2}\frac{\partial^2 u}{\partial y^2}(y - y_c)_2 \quad (1)$$

and

$$v(x,y) = v_c + \frac{\partial v}{\partial y}(y - y_c) + \frac{\partial v}{\partial x}(x - x_c) + \frac{1}{2}\frac{\partial^2 v}{\partial y^2}(y - y_c)^2 + \frac{\partial^2 v}{\partial y \partial x}(y - y_c)(x - x_c) + \frac{1}{2}\frac{\partial^2 v}{\partial x^2}(x - x_c)^2 \quad (2)$$

map the positions within the reference subset to positions in the image after deformation. As illustrated in Fig. 3, u_c and v_c are the displacements of a point at reference image coordinates (x_c, y_c). Here, x and y are the reference coordinates of arbitrary points within the subset centered at (x_c, y_c). The coefficients of the polynomial are optimized by minimizing the normalized cross-correlation coefficient [9], r, defined for an n pixel $\times$ n pixel subset as

$$r = \frac{\sum_{i=1}^{n}\sum_{j=1}^{n} I_1(x_i, y_j) I_2(x_i + u, y_j + v)}{\sum_{i=1}^{n}\sum_{j=1}^{n} \sqrt{I_1^2(x_i, y_j)}\sqrt{I_2^2(x_i + u, y_j + v)}}, \quad (3)$$

where I_1 and I_2 denote the gray level intensity patterns of the reference and deformed images, respectively. Its insensitivity to changes in lighting makes the normalized cross-correlation coefficient an excellent similarity measure. The displacement gradient at the subset center is calculated by evaluating the derivatives $\partial u/\partial x$, $\partial u/\partial y$, $\partial v/\partial x$, and $\partial v/\partial y$ at $(x, y) = (x_c, y_c)$. This algorithm was used to determine the local strain history at individual points on the specimen. Image resolution was 37.5 ('low' magnification) for all front view tests and 75 pixels/mm ('high' magnification via the 200 mm lens extension) for all side view tests. The subsets measured 75 pixels $\times$ 75 pixels. For reference, Fig. 3 shows a subset of size 75 pixels $\times$ 75 pixels at a resolution of 75 pixels/mm.

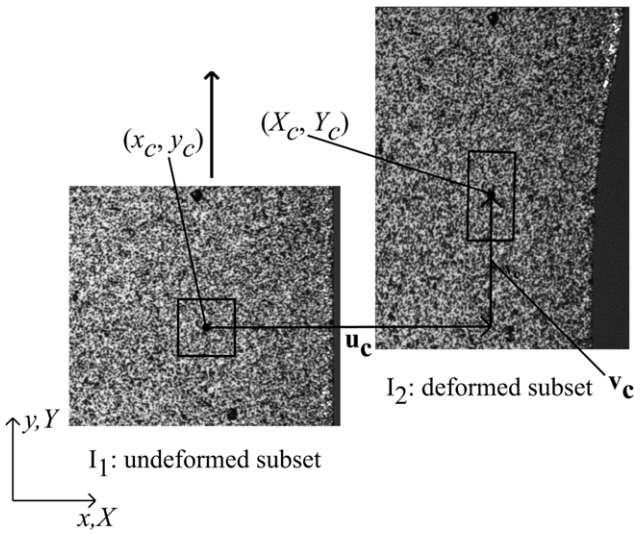

Fig. 3. Illustration of speckle pattern subsets and correlation procedure. Reference coordinates denoted by (x, y), and deformed coordinates denoted by (X, Y).

2.3.1. Local strain calculation

Local lateral vs. axial strain and volumetric strain behaviors were calculated directly from the derivatives of the second-order mapping function described above. Formally, the derivatives define the two-dimensional displacement gradient,

$$\mathbf{H} = \begin{pmatrix} \frac{\partial u}{\partial x} & \frac{\partial u}{\partial y} \\ \frac{\partial v}{\partial x} & \frac{\partial v}{\partial y} \end{pmatrix}, \quad (4)$$

with

$$\mathbf{H} = \mathbf{F} - \mathbf{I}, \quad (5)$$

where $\mathbf{F}$ is the deformation gradient. $\mathbf{F}$ is defined as $\mathbf{I}$ + Grad $\mathbf{u}(\mathbf{x})$, where $\mathbf{x}$ is the position vector of a point in the reference configuration, and $\mathbf{u}(\mathbf{x})$ is the displacement of that point. From the polar decomposition, $\mathbf{F} = \mathbf{VR}$, the true strain in the spatial configuration, or Hencky strain, $\mathbf{E}$, is calculated as

$$\mathbf{E} = \ln \mathbf{V}, \quad (6)$$

where $\mathbf{V}$ is the left stretch tensor and $\mathbf{R}$ is the rotation tensor. The volumetric strain E_{kk} is defined as

$$E_{kk} = \ln \frac{V}{V_o} = \ln(\det \mathbf{F}) \quad (7)$$

where V is the current volume and V_o is the original volume.

2.3.2. Full-field strain calculation

Contours of true axial and shear strain were constructed from the displacement fields. Within the areas of interest, correlations were performed on pixel subsets of size 75 pixels $\times$ 75 pixels at a step size of two. The displacement of the center point of each subset was calculated and stored. The displacement of every second pixel in the area of interest was thus known. The raw full-field displacement data was then imported into MATLAB where the strains were calculated from least-squares approximations of the displacement field. Subsets of the displacement field of size 11 points $\times$ 11 points were taken at a step size of five. A temporary $(\tilde{x}, \tilde{y})$ coordinate system was translated to the

center of each displacement field subset. Second-order polynomial expressions for $u(\tilde{x}, \tilde{y})$ and $v(\tilde{x}, \tilde{y})$ were then fit to each displacement field subset. Similar to the procedure described in Section 2.3.1, the displacement gradient **H** was calculated from the partial derivatives $\partial u/\partial \tilde{x}$, $\partial u/\partial \tilde{y}$, $\partial v/\partial \tilde{x}$, $\partial v/\partial \tilde{y}$ evaluated at each subset center. The logarithmic strain, $\mathbf{E} = \ln \mathbf{V}$, was then calculated and plotted to construct the full-field contours.

2.3.3. Error analysis

There are sources of error in the data acquisition, image correlation, and strain calculation procedures. The error can be separated into noise and systematic components.

A simple test was performed to assess the noise levels in the data acquisition and image correlation procedures. A neat PC tensile specimen was tested with an image resolution of 37.5 pixels/mm and an image acquisition rate of 1 Hz. Before starting the test, a reference image was taken and then 100 additional images were acquired. The specimen was then deformed at a constant nominal strain rate of 0.005 s^{-1} to a crosshead displacement (estimated from prior tests) corresponding to a true axial strain, E_{yy}, of approximately 0.10, and the test was stopped. The image acquisition process was halted for 120 s, and then 100 images were acquired while the specimen was still stationary. The sequence was repeated at strain increments of 0.10 until a maximum strain of approximately 0.50 had been reached. In order to assess the accuracy of the local strain calculation, the images were then analyzed with a subset size of 75 pixels at the lateral center of the specimen at the axial location where necking initiated. As described in Section 2.3.1, E_{yy} was calculated from the raw displacement gradient data via Eq. (6). The very first image acquired was the reference image for all calculations. For the 100 undeformed images, the mean 'apparent' strain was 4 με with a range of 229 με and a standard deviation of 40 με. The baseline accuracy of the local strain measurement is thus on the order of ±100 με. At each subsequent strain, a similar analysis was conducted on the 100 'fixed' images. Due to elastic unloading near the grip regions of the specimen, the strain increased slightly at the point of interest over the course of each set of 100 images. A second-order polynomial was therefore fit to the data at each strain increment, and the range and standard deviation were defined in reference to the polynomial approximation. The range and standard deviation varied from 166 με to 276 με and 34 με to 47 με, respectively, and were not a function of strain. Furthermore, in order to assess the accuracy of the full-field strain calculation as well, the procedure was repeated at a step size of two over a 21 pixel × 21 pixel subset centered on the point described above. Following the algorithm of Section 2.3.2, the displacement gradient at the center of the subset, and in turn the strain, was calculated by fitting quadratic polynomials to the u and v displacements of the resulting 11 × 11 grid. As shown in Fig. 4, the average axial strains (the maximum difference is 340 με) and level of noise measured with the full-field technique are virtually identical to those measured with the local technique.

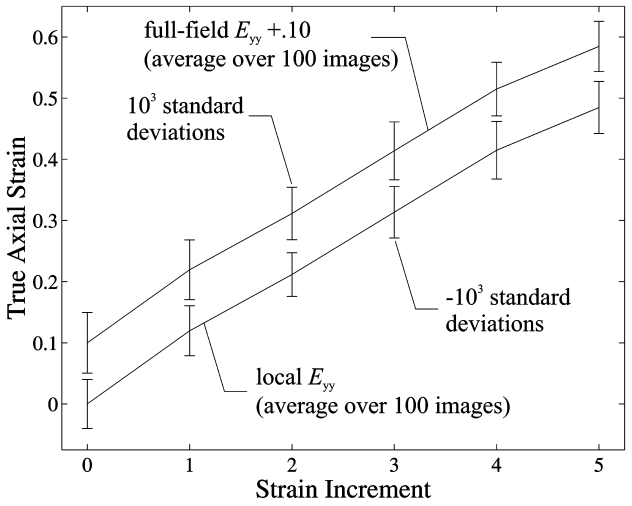

Fig. 4. True axial strain, E_{yy}, measured with the local and full-field techniques as a function of strain. For clarity, the full-field E_{yy} is shifted by 0.10, and the standard deviations are scaled by 10^3.

While the error due to noise is not a function of the strain, it is a strong function of the subset size. Fig. 5 plots the average axial strain and noise level measured with the local technique as a function of correlation subset size at strain increment 3. The image-to-image variability decreases dramatically and the strain approaches a constant value as the subset size increases. At subset sizes greater than 100 pixels, however, the strain begins to decrease indicating that the subset size is too large to capture the strain gradient in the specimen. The subset size of 75 pixels used in all subsequent analyses was thus chosen as a satisfactory compromise between random error and detail lost due to over-smoothing of the data.

The most significant source of systematic error is the 'out-of-plane' error, e, due to the Poisson contraction of the specimen. As the specimen contracts in the x and z directions, the representation of the specimen at the camera

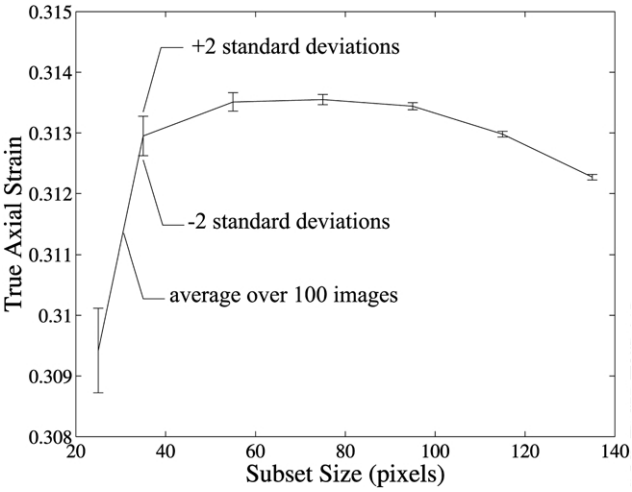

Fig. 5. True axial strain, E_{yy}, as a function of correlation subset size.

sensor becomes smaller. In a coordinate system located at the image center, any point p appears to be at p'. In the y-direction, for example,

$$p'_y \approx \frac{F_0}{F_0 + \mathrm{d}F} \times p_y, \tag{8}$$

where F_0 is the initial distance between the center of the camera lens and the specimen surface (1.0 m) and dF is the out-of-plane displacement. Considering purely axial deformation and approximating the displacement field as linear over the subset, the actual true axial strain can be written as

$$E_{yy} = \ln\left(\frac{p_y^{\mathrm{top}} - p_y^{\mathrm{bot}}}{S-1}\right), \tag{9}$$

where S is the correlation subset size in the case of the local strain calculation and the grid subset size in the case of the full-field strain calculation, and p_y^{top} and p_y^{bot} are the locations of the top and bottom, respectively, of the subset. Similarly, the apparent true axial strain is

$$E'_{yy} = \ln\left(\frac{p_y^{\mathrm{top}'} - p_y^{\mathrm{bot}'}}{S-1}\right). \tag{10}$$

Calculating dF as a function of axial strain by assuming a Poisson's ratio of 0.5, the maximum out-of-plane error is estimated to be 3.5×10^{-3} of the actual value. The maximum error, e, for each strain component from the front and side views are summarized in Table 1.

There are also sources of systematic error due solely to the correlation algorithm itself. In Eq. (3), analytical expressions are developed to represent the discrete matrix of gray level values in each deformed subset. In order to achieve sub-pixel displacement accuracy, I_2 is constructed by evaluating the analytic intensity patterns or 'interpolation functions' at non-integer locations. Schreier et al. [10] have shown that the form of interpolator used in this study, quintic B-spline interpolation, together with a speckle pattern exhibiting a uniform distribution of gray-values, reduces the systematic error (termed interpolation bias) to a level far below that of the measured noise. Systematic error may also arise if the shape functions $u(x, y)$ and $v(x, y)$ which approximate the displacement field are under-matched. Schreier et al. [11] also have shown this error to be insignificant when the shape functions are able to represent accurately the displacement field over the subset and an appropriate speckle pattern is used. For this reason, quadratic shape functions (as opposed to linear) and a relatively small subset size were used in this study.

The total error for a given normal strain component is thus approximated as the random error plus the systematic error due to out-of-plane motion. It takes the form

$$\mathrm{error}(\mu\epsilon) \approx \pm 100 + eE \times 10^6, \tag{11}$$

where E is the appropriate actual strain. The measured strains are clearly very accurate, and the error is significant only at strains similar in magnitude to that of the noise.

Table 1
Maximum out-of-plane strain errors, e, expressed as a fraction of the corresponding actual strain value

	E_{yy} (front)	E_{xx} (front)	E_{yy} (side)	E_{xx} (side)
e	-0.7×10^{-3}	1.4×10^{-3}	-1.7×10^{-3}	3.5×10^{-3}

2.4. True stress calculation

Since no local load or stress information was known, a macroscopic true stress, $\bar{T}_{yy}$, was calculated as

$$\bar{T}_{yy} \equiv \frac{P}{A} = \frac{P}{A_0 \lambda_{xx} \lambda_{zz}}, \tag{12}$$

where P is the load cell measurement, A is the current cross-sectional area of the specimen, A_0 is the initial cross-sectional area of the specimen, and λ_{xx} and λ_{zz} are the macroscopic lateral stretches. λ_{xx} and λ_{zz} were calculated from the change in the specimen's overall width in the x-direction, w, and thickness in the z-direction, t, respectively. As illustrated in Fig. 6,

$$\lambda_{xx} = \frac{w}{w_0} = \frac{X_{\mathrm{L}} - X_{\mathrm{R}}}{x_{\mathrm{L}} - x_{\mathrm{R}}}, \tag{13}$$

with

$$X_{\mathrm{L}} \approx x_{\mathrm{L}} + u(x_{\mathrm{c}}, y_{\mathrm{c}})_{\mathrm{L}} + \left.\frac{\partial u}{\partial x}\right|_{(x_{\mathrm{c}}, y_{\mathrm{c}})_{\mathrm{L}}} (x_{\mathrm{L}} - x_{\mathrm{cL}}), \tag{14}$$

and

$$X_{\mathrm{R}} \approx x_{\mathrm{R}} + u(x_{\mathrm{c}}, y_{\mathrm{c}})_{\mathrm{R}} + \left.\frac{\partial u}{\partial x}\right|_{(x_{\mathrm{c}}, y_{\mathrm{c}})_{\mathrm{R}}} (x_{\mathrm{R}} - x_{\mathrm{cR}}). \tag{15}$$

Similarly,

$$\lambda_{zz} = \frac{t}{t_0} = \frac{Z_{\mathrm{L}} - Z_{\mathrm{R}}}{z_{\mathrm{l}} - z_{\mathrm{r}}}, \tag{16}$$

and so forth.

As will be shown later, the specimens did not deform isotropically in the lateral directions, but the degree of

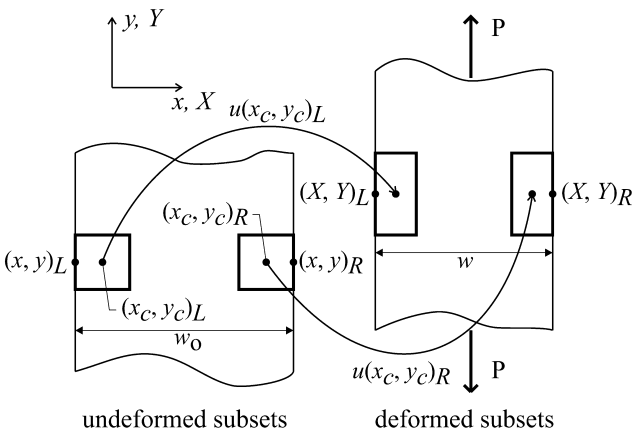

Fig. 6. Definition of variables used in the true stress calculation. Reference coordinates denoted by (x, y), and deformed coordinates denoted by (X, Y).

anisotropy did not significantly affect the true stress calculation. Therefore, with $\lambda_{xx} \approx \lambda_{zz}$, the true stress was taken to be

$$\bar{T}_{yy} \approx \frac{P}{A_0 \lambda_{xx}^2} \tag{17}$$

2.5. Simulations

Due to the inhomogeneous nature of the deformation of polymers during necking, reduction of the accumulated (full-field) specimen data into a measure of the true stress–strain behavior of the material was not straightforward. In order to assess the validity of the procedure and the accuracy of the resulting material true stress–strain behavior, we performed the same data reduction process on a simulation of the inhomogeneous tensile deformation. The simulation allowed us to reduce the simulated specimen data to a material stress–strain behavior and compare the result with the a priori known (input) material stress–strain behavior.

The tensile tests on neat polycarbonate (PC) were simulated with a three-dimensional finite element model. The entire specimen was modeled with 2400 quadratic brick elements. The glassy polymer constitutive model of Boyce et al. [12] as modified by Arruda and Boyce [13] was used to represent the material behavior of PC. In one dimension, the constitutive model can be thought of as a linear elastic spring in series with a parallel arrangement of a viscoplastic dashpot and a non-linear hardening spring. The linear elastic spring provides the initial elastic stiffness of the material. When the material reaches its yield strength, the dashpot is activated enabling viscoplastic flow and strain softening to occur. In this implementation, the evolution equation for the shear strength was modified in order to achieve more gradual post-yield softening. The non-linear hardening spring captures the post-yield strain hardening due to the stretching and orientation of the underlying macromolecular network during viscoplastic flow. The material model parameters were fit to the results of compression tests performed at several different strain rates by Johnson [8]. The tensile yield stress measured in this study was used to calibrate the pressure sensitivity of the model. The analyses were performed with ABAQUS Standard, version 6.3. A geometrically perfect mesh will always deform homogeneously. Therefore, in order to induce the experimentally observed localization, a small edge perturbation, $0.0075w$ deep in the x-direction (as defined in Fig. 2), was created by perturbing a single row of nodes on the positive x-face. The defect was small enough to have no significant effect on the results after necking initiated. Furthermore, the nodes on the x-direction faces were perturbed in accordance with the RMS surface roughness of the specimen, which was measured to be 3 μm with a Zygo interferometer. Further details of the finite element model are provided in Appendix A.

3. Results

3.1. Neat PC: full-field strain contours

Figs. 7(a)–(e) and 8(a)–(e) show experimental contours of true strain, $\mathbf{E} = \ln \mathbf{V}$, for a neat PC tensile bar at crosshead displacements, U, of 2.5, 3.0, 3.5, 4.5, and 7.5 mm. The plots depict the front view of an initially 10 mm long section of the gage length centered at the site of neck initiation (defined as the axial location where the axial strain increased most rapidly). The corresponding load vs. crosshead displacement behavior is shown in Fig. 9.

The plots of axial strain, E_{yy}, in Fig. 7(a) and shear strain, E_{xy}, in Fig. 8(a) shows that the specimen at first deforms uniformly. At $U = 2.5$ mm, corresponding to the peak of the load–displacement curve, the axial strain is approximately constant at $E_{yy} = 0.07$, and the shear strain is non-existent, indicating that the material is still largely in the elastic regime. Soon thereafter, at $U = 3.0$ mm, the load drops as necking begins, and the strain field becomes highly non-uniform. The site of neck initiation is the axial location where, due to some geometric or morphological feature of the specimen, yield occurs first. Localization of plastic flow continues because the decrease in load carried at the first section to yield reduces the load on the rest of the specimen. Apparent in Fig. 7(b)–(d) are the sharp gradients in strain which complicate the measurement of tensile stress–strain behavior in polymers. In Fig. 7(c), the strain ranges from $E_{yy} = 0.1$ to $E_{yy} = 0.5$ over a distance on the order of the specimen width. The inhomogeneous axial strain is accompanied by a sharp increase in the shear strain in Fig. 7(b) and (c). The magnitudes of E_{xy} and the shape of the outline of the specimen are indicative of the sharp, nearly 45°, shear band which rips through the material during neck formation. The deformation remains concentrated in this region until the material in the neck stabilizes, allowing an adjacent section to yield and localize. In Fig. 7(d), the neck has stabilized at a strain of $E_{yy} \approx 0.54$ and begun to propagate along the specimen—behavior commonly referred to as 'cold drawing'. The strain at which the neck stabilizes is termed the 'drawing strain' (calculated as the natural logarithm of the material's draw ratio). The shear band is no longer apparent in Fig. 8(d), but areas of substantial shearing exist near the specimen corners where material is being drawn into the neck. At $U = 7.5$ mm, shown in Figs. 7(e) and 8(e), the neck has propagated nearly the entire length of the portion of the specimen under study. During the whole period of neck propagation, the load–displacement curve is essentially flat. It is not until the neck reaches the grip areas of the specimen at $U \approx 13.0$ mm, and the material begins to strain harden homogeneously, that the load increases again.

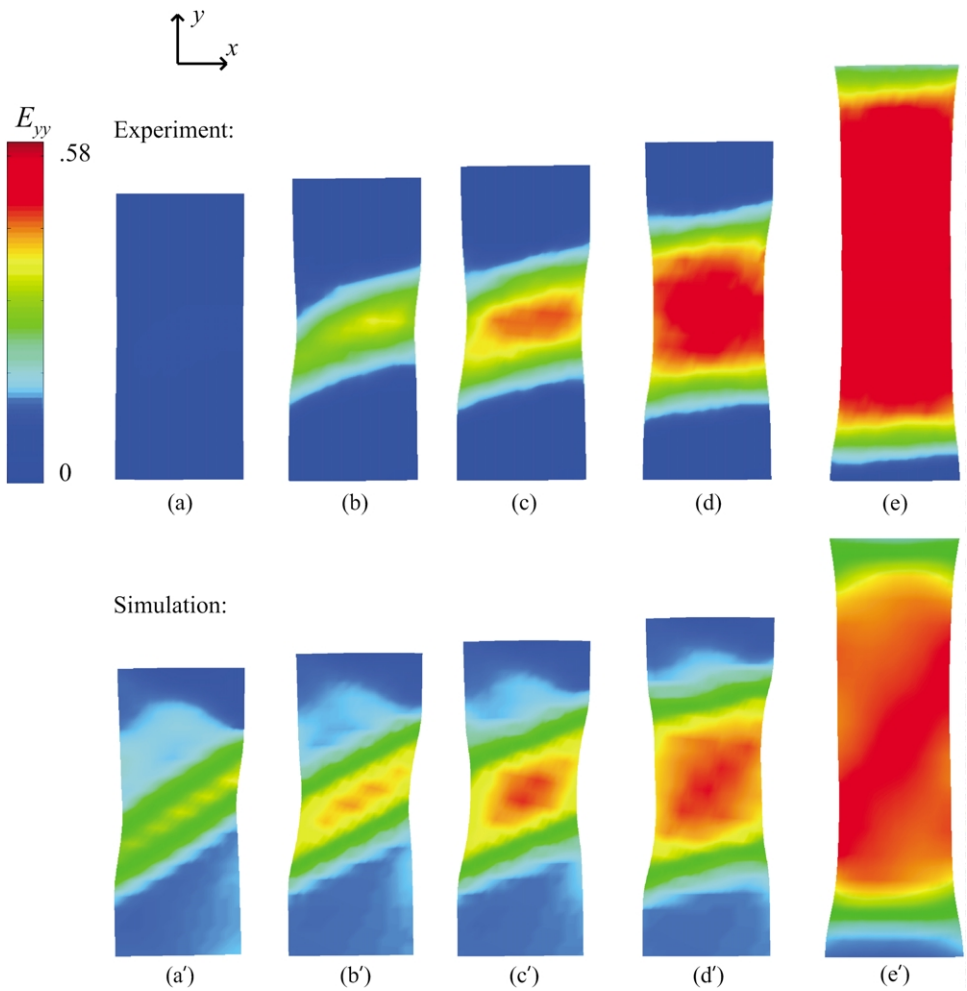

Fig. 7. Experimental (top) and simulated (bottom) uniaxial tension of neat PC (front view). Contours of true axial strain, E_{yy}, for increasing crosshead displacement, U : (a), (a′) $U = 2.5$ mm, (b), (b′) $U = 3.0$ mm, (c), (c′) $U = 3.5$ mm, (d), (d′) $U = 4.5$ mm, (e), (e′) $U = 7.5$ mm.

Figs. 7(a′)–(e′) and 8(a′)–(e′) show the simulation results at crosshead displacements corresponding to those in Figs. 7(a)–(e) and 8(a)–(e). Particularly at large displacements, there is good agreement between the measured and predicted behavior in terms of both strain levels and modes of deformation. The same pattern of localization followed by neck propagation is clearly present. Furthermore, comparing Fig. 7(d) and (d′), one sees that the neck stabilizes in both the experiment and the simulation at nearly the same axial strain. The major difference between the experiment and the simulation is the apparent delayed localization of the experiment. At $U = 2.5$ mm, in Figs. 7(a′) and 8(a′), for example, the simulation has already passed through the peak in the load–displacement curve whereas the experiment has just reached the peak. The experiment yields at a larger crosshead displacement than the simulation (as shown in Fig. 9) in part due to machine compliance, grip alignment, and possible specimen slippage. As will be mentioned later, evidence of these effects also shows itself in a smaller than expected initial true axial strain rate. The discrepancy is also due to the fact that the material model does not capture the pre-peak non-linearity observed in experimental stress–strain curves. Thus, at any given crosshead displacement after the peak load, the simulation is further along in the deformation process than the experiment.

3.2. Neat PC: strain versus time and position

Once necking begins, the behavior of PC becomes a strong function of time and position. Every axial location on the specimen has a unique strain vs. time relationship. In order to characterize most accurately the behavior of PC, the local strain behavior was systematically probed using the algorithm described in Section 2.3. Fig. 10 depicts the matrix of points that were commonly analyzed. Location row 1 is where the neck initiates. Location rows 2, 3, 4, and 5 are 1.0, 2.5, 5.0 and 10.0 mm, respectively, from location row 1. Location column A is at the axial center line of the specimen. Location columns B and C are located one half of the correlation subset size, or 37 pixels, from the edge of the specimen. 37 pixels corresponds to 1.0 mm at low magnification and 0.5 mm at high magnification. Points

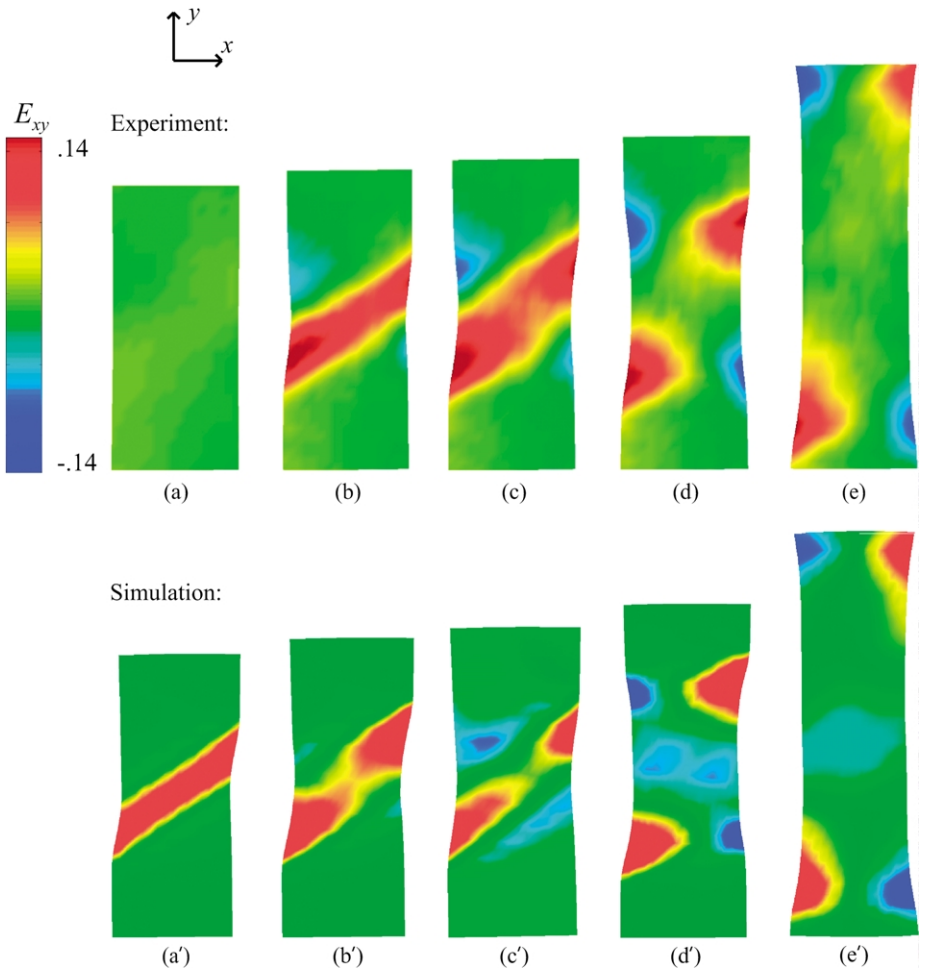

Fig. 8. Experimental (top) and simulated (bottom) uniaxial tension of neat PC (front view). Contours of true shear strain, E_{xy}, for increasing crosshead displacement, U : (a), (a′) $U = 2.5$ mm, (b), (b′) $U = 3.0$ mm, (c), (c′) $U = 3.5$ mm, (d), (d′) $U = 4.5$ mm, (e), (e′) $U = 7.5$ mm.

with subscripts F and S were observed from the front and side views, respectively.

Fig. 11 shows the true axial strain, E_{yy}, vs. time behavior for four points along the front axial center line. In addition, contours of E_{yy} are shown for $t = 50$ s, $t = 100$ s, and

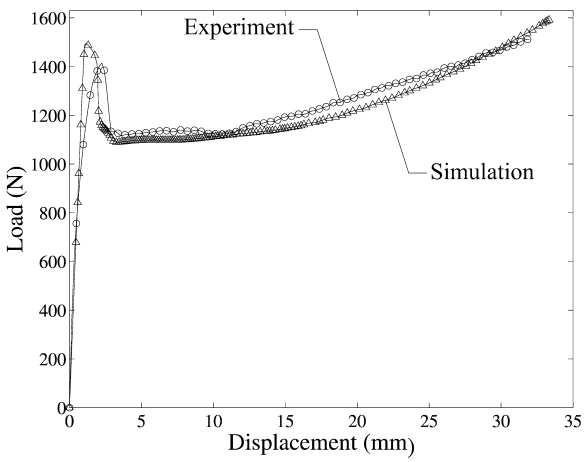

Fig. 9. Uniaxial tension of neat PC. Experimental and simulated load, P, vs. crosshead displacement, U.

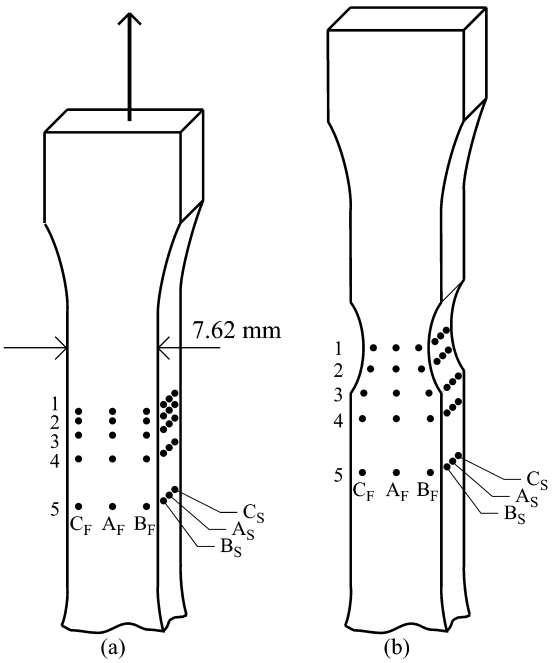

Fig. 10. Definition of strain measurement locations: (a) undeformed specimen, (b) deforming specimen.

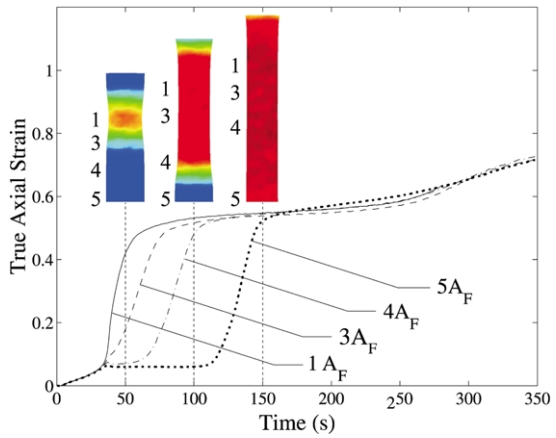

Fig. 11. Uniaxial tension of neat PC (front view). True axial strain, E_{yy}, vs. time and E_{yy} contours at times $t = 50$ s, $t = 100$ s, and $t = 150$ s.

$t = 150$ s. As observed in the full-field strain contours in Section 3.1, the specimen deforms homogeneously at axial strains less than 0.07. Until this point, the axial strain vs. time behavior is identical at all four locations. Once necking begins, however, the curves diverge. At point $1A_F$, the strain rises quickly to the drawing strain of $E_{yy} \approx 0.54$ before essentially leveling off for approximately 200 s. The strain at point $3A_F$, just 1.0 mm from the site of neck formation, rises slightly less rapidly but steadily also to $E_{yy} \approx 0.54$. The strain at points $4A_F$, and $5A_F$, however, plateaus for a period of time before increasing at a rate equal to that of point $3A_F$. During the periods of essentially zero strain rate at points $4A_F$, and $5A_F$, the deformation occurs entirely within the neck. The points a distance away from where the neck forms do not experience plastic deformation until the neck has propagated along the specimen. After leveling off at $E_{yy} \approx 0.54$, all four curves increase in slope again at $t \approx 250$ s. At this time, the neck has propagated to the grip areas of the specimen, and the entire gage length begins to deform homogeneously once again.

Fig. 12 shows the true axial strain vs. time behavior for the three lateral locations, A_F, B_F, and C_F, at axial cross-sections 1, 4, and 5. At location row 1, the axial strain is a function of the lateral position, x. The strain increases more rapidly at the center of the specimen than at the edges. The discrepancy in the strains is due to the fact that location 1 bisects the approximately 45° shear band depicted in Figs. 7(a)–(c) and 8(a)–(c). For the purpose of the true stress–strain calculation, a macroscopic true axial strain, $\bar{E}_{yy}$, was defined at each axial cross-section. The specimen was figuratively sliced in the y-direction into five equally-sized strips. At each axial location, the local axial strains, E_{yy}, at the centers of the five strips were calculated and averaged. Also plotted in Fig. 12 at location rows 1, 4, and 5, $\bar{E}_{yy}$, as expected, lies comfortably between the local E_{yy} measurements. Moving down the specimen away from the point of neck initiation, we see that, at locations rows 4 and 5, the axial strain is approximately constant across the width of the specimen. As illustrated in Fig. 7(d), after neck formation, the shear band quickly disappears, and the axial deformation at a particular cross-section becomes nearly uniform.

The true lateral strain, E_{xx}, vs. time behavior at location rows 1, 4, and 5 is plotted in Fig. 13.

Unlike the axial strain, the lateral strain is a strong function of x at all axial locations. At each location row, the lateral strain is significantly smaller in magnitude at the center of the specimen (location A) than at the edges of the specimen (locations B and C). The strains at locations B and C are nearly identical.

Since the lateral strain is not constant across the width of the specimen, the macroscopic lateral stretch defined in Section 2.4 is used to calculate the current cross-sectional area of the specimen. Fig. 14 shows the local true lateral strain at location row 4 and the macroscopic true lateral strain, $\bar{E}_{xx} = \ln \lambda_{xx}$, with λ_{xx} defined by Eq. (13), plotted as a

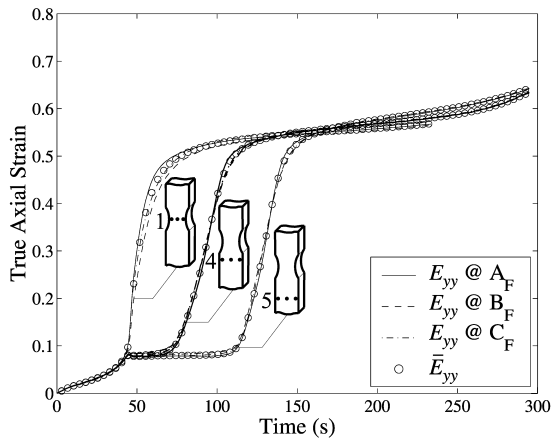

Fig. 12. Uniaxial tension of neat PC (front view). Local true axial strain, E_{yy}, and macroscopic true axial strain, $\bar{E}_{yy}$, vs. time at location rows 1, 4, and 5.

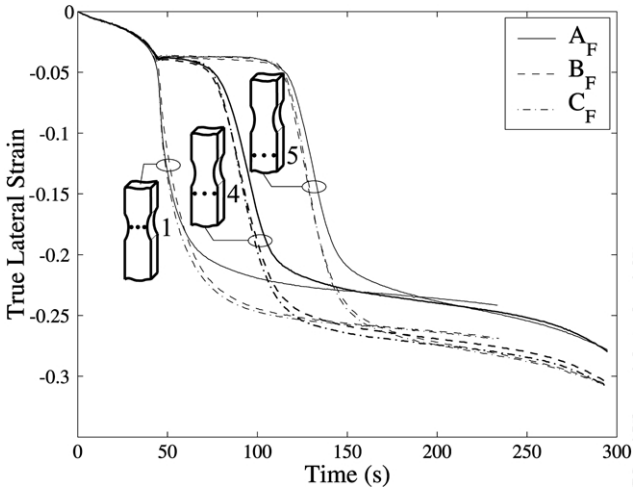

Fig. 13. Uniaxial tension of neat PC (front view). Local true lateral strain, E_{xx}, vs. time at location rows 1, 4, and 5.

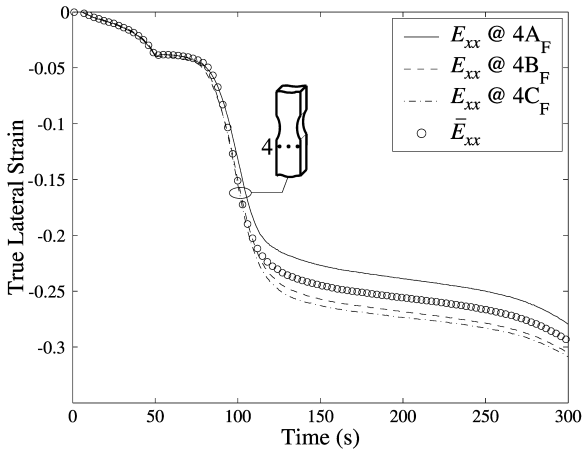

Fig. 14. Uniaxial tension of neat PC (front view). Local true lateral strain, E_{xx}, and macroscopic true lateral strain, $\bar{E}_{xx}$, vs. time at location row 4.

function of time. The macroscopic curve fits nicely between the responses of the sides and the center.

Fig. 15 is a plot identical to Fig. 14 but with the measurements taken from the side view of the specimen. The macroscopic strain again falls between the three local strain measurements.

Combining the results from this section, we plot the macroscopic true lateral strain vs. macroscopic true axial strain at locations 3_F and 3_S in Fig. 16.

The initial slopes of these curves define the elastic Poisson's ratios, ν_{yx} and ν_{yz}. Both equal to 0.39, the values of ν_{yx} and ν_{yz} indicate that the specimen deforms in a transversely isotropic manner. Henceforth, the Poisson's ratio will thus be referred to as simply ν. At larger strains, however, the specimen does not deform isotropically in the two lateral directions. The specimen contracts more in the z-direction, particularly at axial strains greater than 0.25. While the degree of anisotropy is small enough to have virtually no effect on the true stress calculation (hence Eq. (17)), as will be shown in Section 3.4, the anisotropy must be taken into consideration when calculating the volumetric strain.

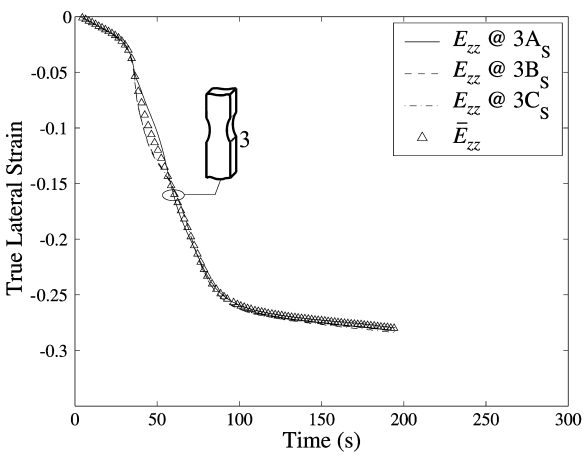

Fig. 15. Uniaxial tension of neat PC (side view). True lateral strain, E_{zz}, and macroscopic true lateral strain, $\bar{E}_{zz}$, vs. time at location row 3.

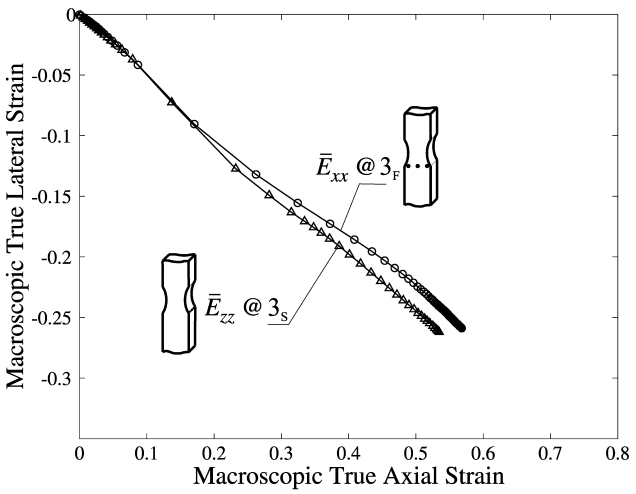

Fig. 16. Uniaxial tension of neat PC. Macroscopic true lateral strains, $\bar{E}_{xx}$ and $\bar{E}_{zz}$, vs. macroscopic true axial strain, $\bar{E}_{yy}$.

3.3. Neat PC: true axial stress–strain behavior

One of the primary goals of this study was to determine the constant strain rate constitutive behavior of PC in uniaxial tension from a standard tension test. It is well known that the response of polymers is a strong function of time due to the strain rate dependency of yield and the phenomenon of stress relaxation. Figs. 11 and 12 show that the axial strain vs. time behavior is different for every axial location on the specimen. It follows that the stress–strain behavior must also be a function of axial location. Furthermore, even at a particular axial location, the true axial strain rate is a function of axial strain. In order to determine how best to infer a single representative stress–strain curve from a test where every material point behaves differently, the simulation was consulted. It is shown how the constitutive behavior of PC in uniaxial tension—viewed as a known in the simulation—can be 'backed out' from the same macroscopic quantities that the experimental technique measures.

Fig. 17 shows the simulation's macroscopic true axial strain rate, $\dot{\bar{E}}^{\mathrm{ip}}_{yy}$, at axial locations 1, 3, and 5 as a function of time.

$\dot{\bar{E}}^{\mathrm{ip}}_{yy}$ is given by

$$\dot{\bar{E}}^{\mathrm{ip}}_{yy} \equiv \frac{\bar{E}^{\mathrm{ip}}_{yy}|_{t_{i+1}} - \bar{E}^{\mathrm{ip}}_{yy}|_{t_i}}{t_{i+1} - t_i}, \tag{18}$$

where $\bar{E}^{\mathrm{ip}}_{yy}$ is the axial strain averaged over all integration points "ip's" at a given axial cross-section in the reference configuration. Over the three axial locations, $\dot{\bar{E}}_{yy}$ is constant during only the first few seconds of the test. Here, the material is still in the initial, elastic regime. Thereafter, the strain rate jumps an order of magnitude at location 1 as the neck forms. While the neck is at location 1, $\dot{\bar{E}}_{yy}$ at location 3 decreases, but remains positive, as material is slowly drawn into neck, but, at location 5, $\dot{\bar{E}}_{yy}$ decreases to

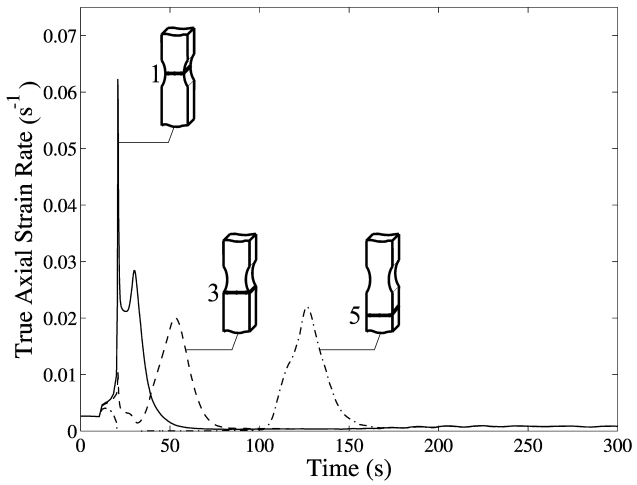

Fig. 17. Tensile bar simulation results for uniaxial tension of neat PC. Macroscopic true axial strain rate, $\bar{\dot{E}}^{ip}_{yy}$, vs. time at axial locations 1, 3, and 5.

slightly less than zero due to elastic unloading in the wake of the macroscopic load drop. This period of approximately constant axial strain was observed in the experimental results presented in Figs. 11 and 12. Once the drawing strain is reached at location 1, the neck propagates and the strain rate falls to essentially zero. Locations 3 and 5 undergo similar strain rate jumps when the neck reaches their vicinity. Eventually, at $t \approx 170$ s, the neck reaches the grip areas of the specimen, and the entire gage length begins to deform homogeneously again at a rate of approximately 0.0015 s^{-1}. Every material point thus experiences an over two orders of magnitude variation in strain rate over the course of a constant crosshead velocity test.

Fig. 18 illustrates the relationship in the simulation between stress–strain behavior and strain rate.

The macroscopic true axial stress, $\bar{T}^{ip}_{yy}$, analogous to $\bar{E}^{ip}_{yy}$, is the true axial stress averaged over all integration points at a

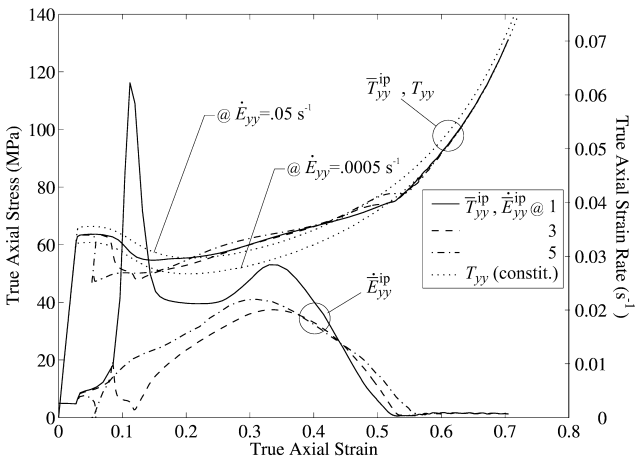

Fig. 18. Tensile bar simulation results for uniaxial tension of neat PC. Macroscopic true axial stress, $\bar{T}^{ip}_{yy}$, (left hand axis) and macroscopic true axial strain rate, $\bar{\dot{E}}^{ip}_{yy}$, (right hand axis) vs. macroscopic true axial strain, $\bar{E}^{ip}_{yy}$, at axial locations 1, 3, and 5. Constitutive model true axial stress, T_{yy}, vs. true axial strain, E_{yy}, at true strain rates $\dot{E}_{yy} = 0.0005$ s^{-1} and $\dot{E}_{yy} = 0.05$ s^{-1}.

particular axial cross-section. In order to evaluate how well the measured behavior represents the material's actual uniaxial stress–strain behavior, the true stress–strain behavior predicted by the constitutive model for homogeneous uniaxial tension at strain rates of 0.0005 s^{-1} and 0.05 s^{-1} is also plotted in Fig. 18.

Locations 1, 3, and 5 exhibit, particularly at intermediate strains, significantly different stress–strain behavior due to their disparate strain rate histories. The strain rate is not a function of position until after yielding, however, and hence all three locations yield at 65 MPa. At yield, the strain rate is close to 0.005 s^{-1}, and, in fact, the measured yield stress sits squarely between the yield stresses predicted by the constitutive model for strain rates of 0.0005 s^{-1} and 0.05 s^{-1}. After yield, the rate of softening increases with the distance from the site of neck initiation. At location 1, the strain rate jumps by an order of magnitude and the stress–strain curve correspondingly shifts up nearly to the prediction for $\dot{E}_{yy} = 0.05$ s^{-1}. At strains larger than $\bar{E}_{yy} = 0.33$, the strain rate at location 1 steadily decreases to approximately 0.0005 s^{-1}, and the stress–strain curve follows suit by gradually transitioning to the behavior predicted for a strain rate of 0.0005 s^{-1}. Here, the decrease in strain rate is in competition with the material's tendency to harden. Once the neck stabilizes at $\bar{E}^{ip}_{yy} \approx 0.54$, the strain rate goes to zero as the neck propagates along the specimen. The strain rate at location 3 deviates from that at location 1 soon after yield. The decrease to a minimum of nearly zero exaggerates the softening response and causes a rather sudden drop in the stress level below that predicted for $\dot{E}_{yy} \approx 0.0005$ s^{-1}. Once the neck begins to propagate, the strain rate at location 3 increases and the behavior follows the pattern of location 1. The behavior at location 5 follows the same trend as locations 1 and 3, but, in this case, as illustrated in Fig. 17, the strain rate falls to zero or less for over 60 s and elastic unloading occurs. The elastic unloading is readily apparent in Fig. 18 as the slope of the stress–strain curve during the stress drop is parallel to the slope during the elastic regime. Finally, all three stress–strain curves exhibit a 'kink' at $\bar{E}^{ip}_{yy} \approx 0.54$ coincident with the neck reaching the grip areas and the reestablishment of homogeneous deformation. This phenomenon is due to the fact that, after the neck propagates through, all sections but the last to localize experience a period of stress relaxation followed by a strain rate jump from zero to approximately 0.0015 s^{-1}.

For the most part, all three curves are bracketed by the constitutive behavior at $\dot{E}_{yy} = 0.0005$ s^{-1} and $\dot{E}_{yy} = 0.05$ s^{-1}. Overall, when strain rate effects are included, the average stress and strain in a tensile bar is shown to represent adequately the material stress–strain behavior. The experimental technique, however, is not privy to the stress and strain at interior points. It can only measure the average stress in the material and the surface strains. In order to demonstrate the accuracy of the present

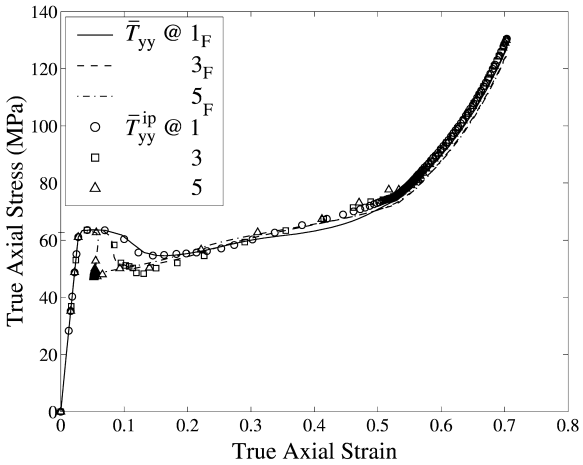

Fig. 19. Tensile bar simulation results for uniaxial tension of neat PC. Macroscopic true axial stress, $\bar{T}_{yy}$, vs. macroscopic true axial strain, $\bar{E}_{yy}$, and macroscopic true axial stress, $\bar{T}^{ip}_{yy}$, vs. macroscopic true axial strain, $\bar{E}^{ip}_{yy}$, at axial locations 1, 3, and 5.

technique, in Fig. 19, the average stress–strain behavior, calculated as above using all integration points at a cross-section ($\bar{T}^{ip}_{yy}$–$\bar{E}^{ip}_{yy}$) is compared to the average stress–strain behavior ($\bar{T}_{yy}$–$\bar{E}_{yy}$) evaluated using the variables actually measured during the experiments. Specifically, $\bar{T}_{yy}$ is calculated from Eq. (17), with P given by the sum of the nodal reaction forces at the grip. $\bar{E}_{xx}$ is calculated as $\ln \lambda_{xx}$, with λ_{xx} taken from Eq. (13), with x_{2L} and x_{2R} given by the nodal displacements on the edges of the bar. $\bar{E}_{yy}$ is calculated from the axial strains at five equi-spaced integration points near the surface of the bar. The excellent agreement between the two sets of stress–strain curves shown in Fig. 19 proves that the assumptions of the experimental technique are valid.

The experimentally measured stress–strain and strain rate data depicted in Fig. 20 exhibits the same trends

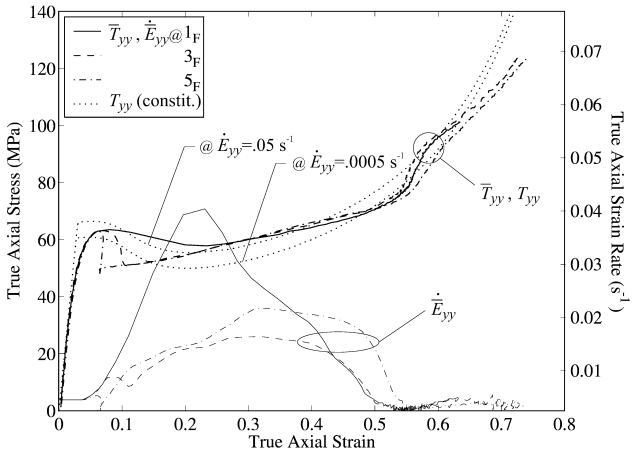

Fig. 20. Experimental results for uniaxial tension of neat PC. Macroscopic true axial stress, $\bar{T}_{yy}$, (left hand axis) and macroscopic true axial strain rate, $\dot{\bar{E}}_{yy}$, (right hand axis) vs. macroscopic true axial strain, $\bar{E}_{yy}$ at axial locations 1_F, 3_F, and 5_F. Constitutive model true axial stress, T_{yy}, vs. true axial strain, E_{yy}, at true strain rates $\dot{E}_{yy} = 0.0005\ s^{-1}$ and $\dot{E}_{yy} = 0.05\ s^{-1}$.

observed in the simulation, but there are minor discrepancies. As alluded to in Section 3.1, the initial axial strain rate, when the deformation is still homogeneous, is smaller than expected due to factors related to the load frame and grips. The stress–strain behavior at location 1_F softens less and at a rate slower than that of the simulation. This is likely due to the peak in strain rate at location 1_F being substantially broader in the experiment than in the simulation (Fig. 18). As observed in Figs. 7 and 8 and discussed in Section 3.1, the shear band in the simulation is sharper than the shear band that forms during the experiment. The greater degree of localization of course implies a higher strain rate. The experimental and simulation results also differ at large axial strains. The experimental stress–strain curves exhibit a sharper kink at $\bar{E}_{yy} \approx 0.54$ and a lower rate of hardening. This is, at least in part, an artifact of the choice of material model parameters used in the simulation. Due to an increasingly gradual transition from localized deformation to homogeneous deformation, the magnitude of the kink in the experimental stress–strain curve decreases as the measurement location is moved away from the point of neck initiation. Fig. 11 shows that, immediately after neck stabilization, the strain at point $5A_F$ increases almost monotonically while the strain at locations closer to the site of neck formation remains almost constant. Correspondingly, in Fig. 20, at large axial strains, the strain rate at point 5_F remains positive. After the drawing strain is reached, the strain rate at locations 1_F and 3_F, however, is nearly zero until the neck reaches the grip area.

The fact that the strain rate vs. axial strain relationship is different at every axial location on the specimen is used to approximate the constant strain rate true stress–strain behavior of the material. Every point on the specimen gage length eventually experiences the entire range of axial strains. A composite stress–strain curve based on strain rate can therefore be constructed from the results at any number of axial locations. This was accomplished, in a manner similar to that described in Section 2.3.2, by performing the correlation, macroscopic true stress–strain calculation, and macroscopic strain rate calculation at every fourth axial pixel location (for a total of approximately 100). The results were then interpolated to coincide with 40 macroscopic axial strains spaced equally between $\bar{E}_{yy} = 0$ and $\bar{E}_{yy} = 0.75$. The behavior chosen to represent each axial strain was drawn from the axial location which exhibited a strain rate closest to a designated target rate. Fig. 21 illustrates the locations and strain rates chosen for a target rate of $\dot{\bar{E}}_{yy} = 0.02\ s^{-1}$. For clarity, the strain rate vs. axial strain behavior at only four locations is shown, but it is apparent how the composite strain rate curve transitions from the behavior at location 1_F at small axial strains to the behavior at location 5_F at large axial strains. The target rate was chosen to maximize the width of the constant strain rate plateau while avoiding any strain rate drops during the early stages of deformation. While the strain rate is thus kept constant during much of the period of neck propagation, it is

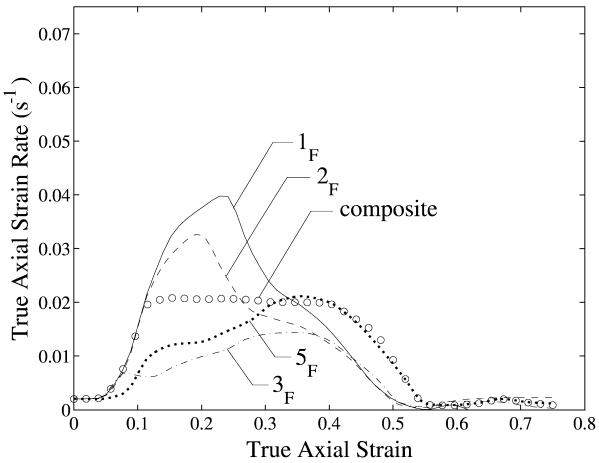

Fig. 21. Uniaxial tension of neat PC. Macroscopic true axial strain rate, $\dot{\bar{E}}_{yy}$, vs. true axial strain, $\bar{E}_{yy}$, at axial locations 1_F, 2_F, 3_F, and 5_F and composite curve.

impossible to maintain a constant strain rate for all axial strains due to the large disparity in strain rates experienced over the course of a test.

The macroscopic stress–strain curves corresponding to the strain rate curves in Fig. 21, together with the constitutive behavior at $\dot{E}_{yy} = 0.02\ s^{-1}$, are shown in Fig. 22.

The composite macroscopic stress–strain curve transitions nicely from the results at location 1_F to those at location 5_F. While the target strain rate is maintained, there is excellent agreement between the composite behavior and the constitutive model prediction. Because, at large axial strains, it takes on the behavior of the point on the gage section furthest from the site of neck formation, the composite curve also successfully avoids the kinking phenomenon.

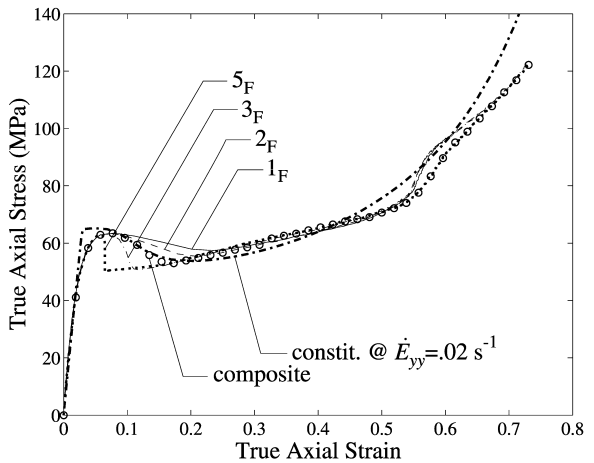

Fig. 22. Uniaxial tension of neat PC. Macroscopic true axial stress, $\bar{T}_{yy}$, vs. true axial strain, $\bar{E}_{yy}$ at axial locations 1_F, 2_F, 3_F, and 5_F and composite curve. Constitutive model true axial stress, T_{yy}, vs. true axial strain, E_{yy}, at true strain rate $\dot{E}_{yy} = 0.02\ s^{-1}$.

3.4. Neat PC: volumetric behavior

The final goal of this study was to measure the volume change during a tensile test. In general, volumetric strain is an important measure for quantifying modes of deformation and/or identifying events such as debonding or cavitation. An amorphous, non-crazing polymer, polycarbonate is known to conserve volume during plastic deformation. The material's incompressibility and the constraints of the specimen geometry cause the tensile bar to laterally deform in an inhomogeneous manner. The inhomogeneity is readily apparent upon examination of the surface of a deformed specimen. From the front view, the surface exhibits an out-of-plane concave shape with the largest through-thickness macroscopic strains ($\bar{E}_{zz}$) occurring at the center, along the y-axis. This observation is in accord with Fig. 13 which shows that E_{xx} is at a minimum (in magnitude) at $x = 0$. Therefore, the current area is slightly overestimated in Eqs. (12) and (17), which assume that $\bar{E}_{zz}$ is constant across the specimen width. While negligible when calculating the true stress, the error in the current area calculation prohibits determining the volumetric strain from macroscopic measurements. Very small in PC and a function of the change in area (not the area itself as in the case of the true stress), the volumetric strain is significantly overestimated by a macroscopic calculation.

Thus, for the volumetric strain, a local measurement and Eq. (7) are used. The shape of the deformed specimens and the lateral strain behavior presented in Figs. 13 and 16 indicate that, even locally, the material does not deform isotropically in the two transverse directions. Since the current technique can only measure in-plane strains, the simulation was used to evaluate the degree of anisotropy and determine how best to measure the volumetric strain. Fig. 23 shows that, at point $1B_F$, for example, the strains in the z-direction are substantially larger in magnitude than those in the x-direction. Assuming that the quantity

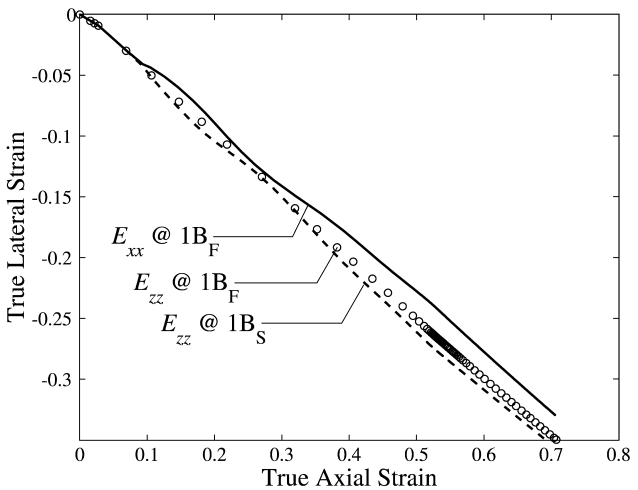

Fig. 23. Tensile bar simulation results for uniaxial tension of neat PC. True lateral strains, E_{xx} and E_{zz}, vs. true axial strain, E_{yy}, at axial location 1B.

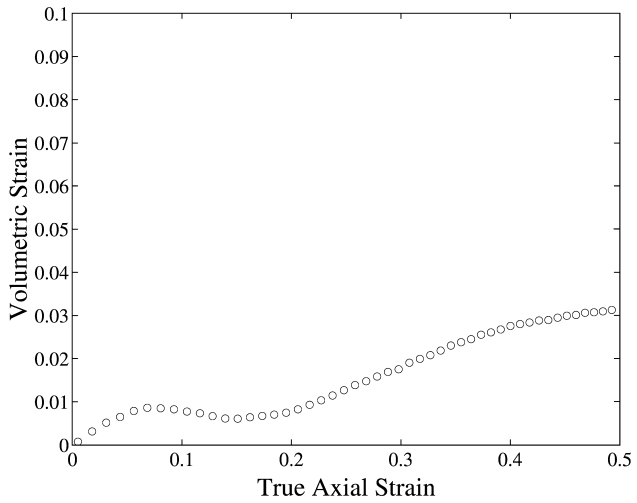

Fig. 24. Uniaxial tension of Neat PC. Volumetric strain, E_{kk}, vs. true axial strain, E_{yy}.

measurable from the front view, E_{xx}, is identical to E_{zz} would thus overestimate the volume change. Fig. 23, however, also indicates that the through-thickness lateral strain, E_{zz}, vs. axial strain behavior at point $1B_S$ is nearly identical to that at point $1B_F$. Since it is impossible to measure both E_{xx} and E_{zz} at the same location, points $1B_F$ and $1B_S$ were assumed to represent approximately the same material point. The behavior measured on the z-plane at $1B_F$ and the behavior measured on the x-plane at $1B_S$ were combined in order to evaluate the volume change via Eq. (7).

Using two tests to represent one test introduces additional sources of error. The simulation showed that the results at points $1B_F$ and $1B_S$ accurately represent the behavior of a single material point. The experimental results, however, must be taken from separate tests, and unfortunately no two specimens deform identically. Furthermore, it is impossible to know whether one is correlating $1B_F$ with $1B_S$ or $1B_F$ with $1C_S$, and so forth. Therefore, from each perspective, up to six tests were performed, and the results at points 1B and 1C were interpolated and averaged for each axial strain, E_{yy}, to form the mean displacement gradients $\bar{\mathbf{H}}^F$ and $\bar{\mathbf{H}}^S$. $\bar{\mathbf{H}}^F$ and $\bar{\mathbf{H}}^S$ were correlated at each axial strain, and the deformation gradient was defined as

$$\mathbf{F} = \begin{pmatrix} \bar{H}^F_{xx} + 1 & \bar{H}^F_{xy} & 0 \\ \bar{H}^F_{yx} & (\bar{H}^F_{yy} + \bar{H}^S_{yy})/2 + 1 & \bar{H}^S_{yz} \\ 0 & \bar{H}^S_{zy} & \bar{H}^S_{zz} + 1 \end{pmatrix}. \tag{19}$$

The volumetric strain calculated from Eq. (7) for uniaxial tension of neat PC is shown in Fig. 24.

At small strains, the volumetric strain increases linearly due to the elastic Poisson effect. At $E_{yy} \approx 0.07$, the volume change levels off at approximately 0.01 as the mode of deformation switches to incompressible plastic flow. Immediately thereafter, the volumetric strain decreases slightly. The decrease in volume is likely due to elastic recovery as the stress level drops during the strain softening stage of deformation. At $E_{yy} \approx 0.20$, the volumetric strain increases again before finally leveling off at approximately 0.03 at $E_{yy} = 0.50$. Further dilatation is attributed to the additional elastic deformation which occurs during the strain hardening stage of deformation and possible small-scale cavitation events at defects (such as dust particles) in the material.

The maximum error in the volumetric strain calculation is approximated from Eqs. (7) and (11) by neglecting the shear strains and assuming that the noise acts in the same direction as the out-of-plane error (i.e. minimizing E_{yy} and maximizing E_{xx} and E_{zz}). The error ranges almost linearly from $-300\ \mu\epsilon$ at $E_{yy} = 0$ to $-2100\ \mu\epsilon$ at $E_{yy} = 0.5$. Even at its absolute theoretical maximum, this error is only roughly 10% of E_{kk} and is within acceptable bounds.

3.5. Rubber-filled PC

The full-field strain contour, macroscopic stress–strain, and volumetric strain analyses described in the previous sections were also conducted on blends with rubber volume fractions of $f = 0.05$, $f = 0.15$, and $f = 0.25$.

3.5.1. Full-field strain contours

Contours of true axial and shear strain for the three rubber-filled blends are plotted in Figs. 25–30. The axial strain contours for blends with $f = 0.05$ and $f = 0.15$, shown in Figs. 25 and 27, respectively, are remarkably similar to those of the neat polymer. The shear strain contours for $f = 0.05$ in Fig. 26 and, particularly, for $f = 0.15$ in Fig. 28, however, show substantially less shear deformation than the contours for the neat material in Fig. 8. The rubber particles stabilize the deformation and, as their volume fraction increases, inhibit the sudden shear band formation which occurs in the homopolymer. The axial strains in the homopolymer are actually slightly lower than those in the blends with $f = 0.05$ and $f = 0.15$ due to the amount of axial displacement accommodated by the shear band.

The behavior of the blend with $f = 0.25$ is completely different than that of the homopolymer and the blends with a lower volume fraction of filler. The contours of axial strain in Fig. 29 depict a pattern of deformation substantially more uniform than that observed in any of the other materials. The plots of shear strain in Fig. 30 show negligible shearing except where material is being drawn into the neck. The neck itself is not nearly as sharp, nor are the peak axial strain levels as high, as in the other blends or the homopolymer. As will be further discussed below in Section 3.5.2, yield stress and post-yield strain softening decrease with increasing f. These factors combine to reduce the localization phenomenon, resulting in a substantially more homogeneous deformation at large f.

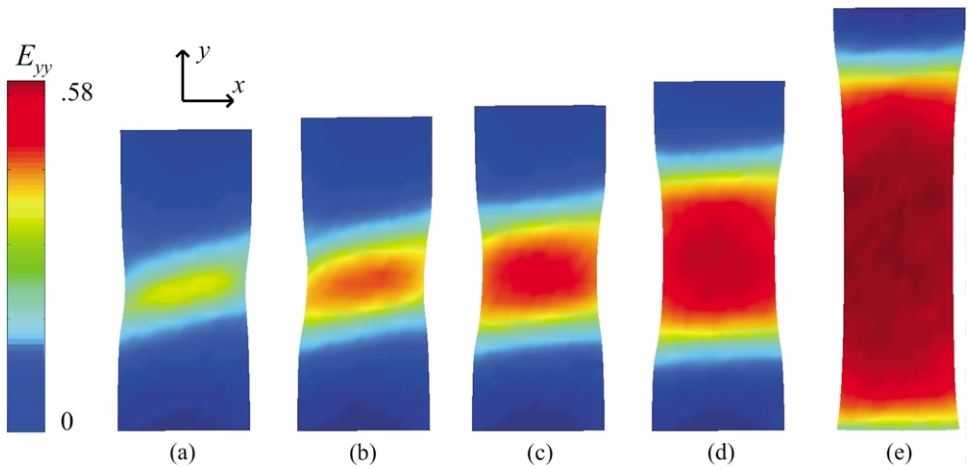

Fig. 25. Experimental uniaxial tension of rubber-filled PC, $f = 0.05$ (front view). Contours of true axial strain, E_{yy}, for increasing crosshead displacement, U : (a) $U = 2.5$ mm, (b) $U = 3.0$ mm, (c) $U = 3.5$ mm, (d) $U = 4.5$ mm, (e) $U = 7.5$ mm.

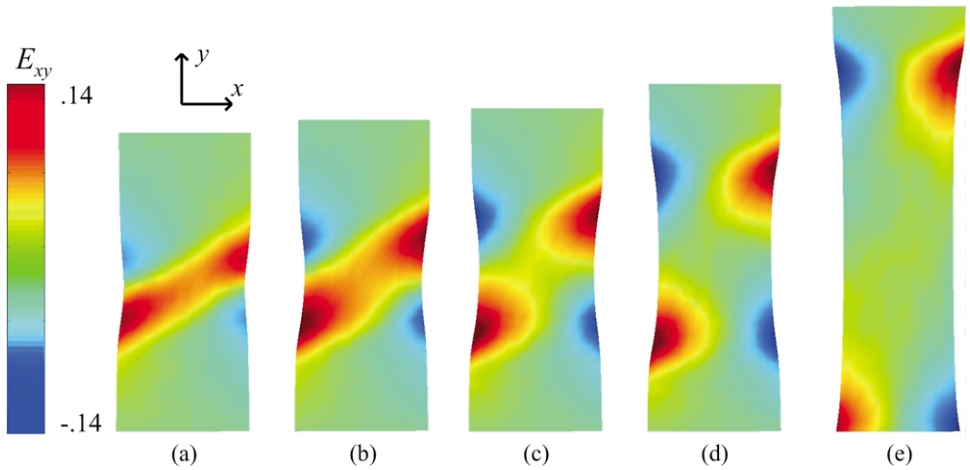

Fig. 26. Experimental uniaxial tension of rubber-filled PC, $f = 0.05$ (front view). Contours of true shear strain, E_{xy}, for increasing crosshead displacement, U : (a) $U = 2.5$ mm, (b) $U = 3.0$ mm, (c) $U = 3.5$ mm, (d) $U = 4.5$ mm, (e) $U = 7.5$ mm.

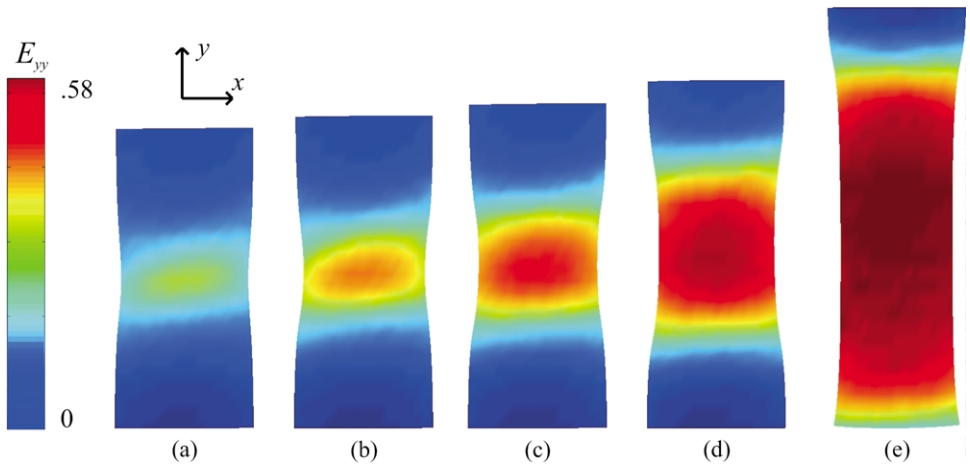

Fig. 27. Experimental uniaxial tension of rubber-filled PC, $f = 0.15$ (front view). Contours of true axial strain, E_{yy}, for increasing crosshead displacement, U : (a) $U = 2.5$ mm, (b) $U = 3.0$ mm, (c) $U = 3.5$ mm, (d) $U = 4.5$ mm, (e) $U = 7.5$ mm.

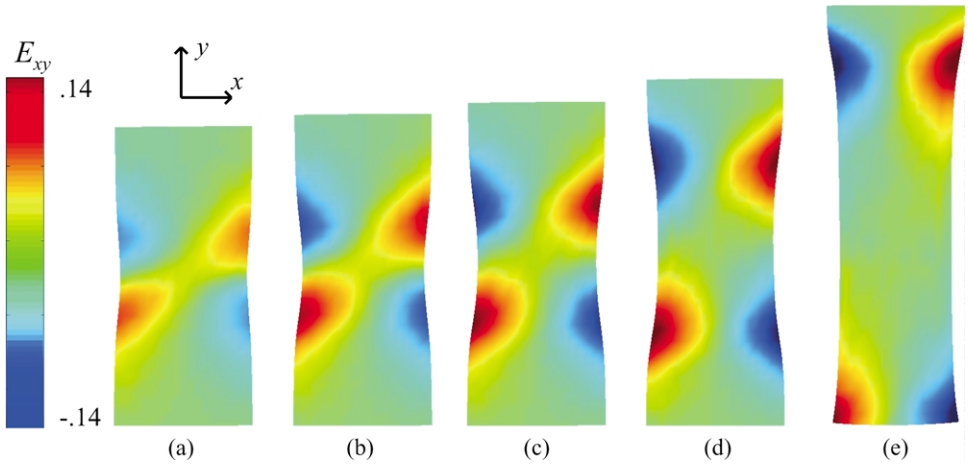

Fig. 28. Experimental uniaxial tension of rubber-filled PC, $f = 0.15$ (front view). Contours of true shear strain, E_{xy}, for increasing crosshead displacement, U : (a) $U = 2.5$ mm, (b) $U = 3.0$ mm, (c) $U = 3.5$ mm, (d) $U = 4.5$ mm, (e) $U = 7.5$ mm.

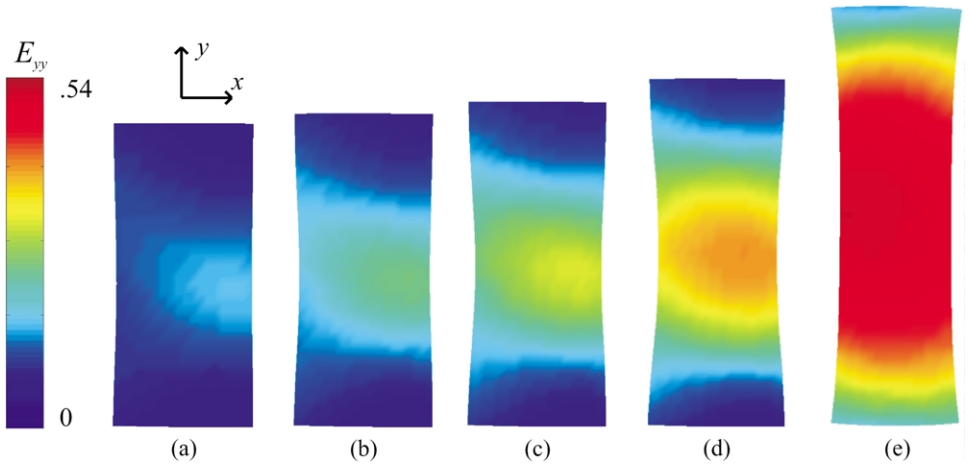

Fig. 29. Experimental uniaxial tension of rubber-filled PC, $f = 0.25$ (front view). Contours of true axial strain, E_{yy}, for increasing crosshead displacement, U : (a) $U = 2.5$ mm, (b) $U = 3.0$ mm, (c) $U = 3.5$ mm, (d) $U = 4.5$ mm, (e) $U = 7.5$ mm.

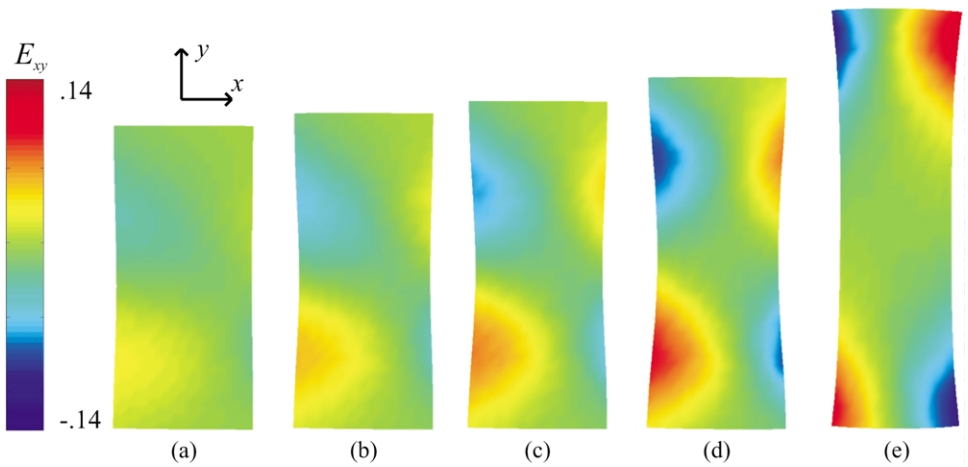

Fig. 30. Experimental uniaxial tension of rubber-filled PC, $f = 0.25$ (front view). Contours of true shear strain, E_{xy}, for increasing crosshead displacement, U : (a) $U = 2.5$ mm, (b) $U = 3.0$ mm, (c) $U = 3.5$ mm, (d) $U = 4.5$ mm, (e) $U = 7.5$ mm.

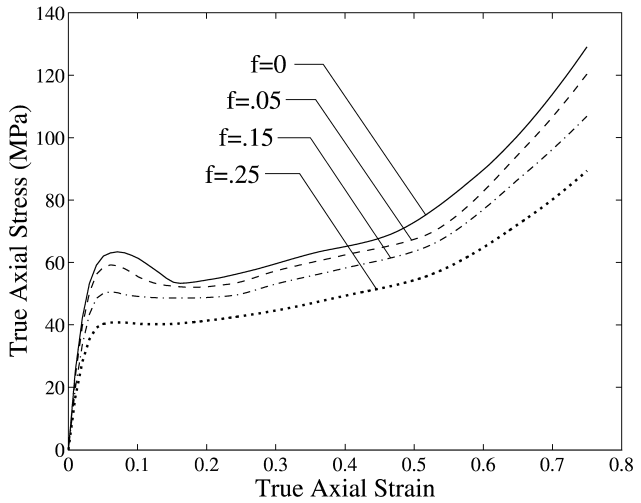

Fig. 31. Uniaxial tension of neat and rubber-modified PC. Macroscopic true axial stress, $\bar{T}_{yy}$, vs. true axial strain, $\bar{E}_{yy}$.

3.5.2. True axial stress–strain behavior

Fig. 31 displays the composite macroscopic true stress–strain curves for the homopolymer and the three blends while Fig. 32 illustrates the true axial strain rates associated with each composite curve.

As the rubber volume fraction increases, the degree of localization and maximum strain rate decrease, allowing a smaller target strain rate to be chosen. In fact, with a target strain rate of $\dot{\bar{E}}_{yy} = 0.007\ s^{-1}$, the composite curves for $f = 0.15$ and $f = 0.25$ achieve an almost constant true strain rate. The stress–strain curves in Fig. 31 exhibit the expected decrease in modulus and yield stress with increasing rubber volume fraction. The elastic properties of the blends agree closely with the predictions of the composite model of Mori and Tanaka [14]. Details of the model and the specific form used can be found in Appendix B. The predicted ratios of blend modulus to neat modulus, E_{blend}/E, for volume fractions of $f = 0.05$, $f = 0.15$, and $f = 0.25$, are 0.92, 0.77, and 0.64, respectively, while the measured ratios are 0.94, 0.77, and 0.63, respectively. Also calculated for each material from the elastic part of the true macroscopic axial vs. lateral strain curve is the Poisson's ratio, ν. Possessing a Poisson's ratio approaching 0.5, the rubber particles increase the Poisson's ratios of the blends. The predicted Poisson's ratios, for volume fractions of $f = 0.05$, $f = 0.15$, and $f = 0.25$, are 0.398, 0.409, and 0.420, respectively, while the measured values are 0.397, 0.414, and 0.423. Averaged over a minimum of four tests for each volume fraction, the yield stresses and elastic properties are summarized in Table 2. Furthermore, consistent with the compression data of Johnson [8] and the micromechanical modeling of Danielsson et al. [15], the stress–strain data exhibits a decrease in post-yield strain softening and, at large strains, strain hardening slope with increasing rubber volume fraction. The reduction in rate and magnitude of post-yield softening with increasing f correlates well with the increasingly homogeneous deformation observed with increasing f in the full-field strain contours. As discussed in Section 3.1, the axial location where necking initiates is the first to yield. The instability is due to the inability of the material's plastic resistance to balance the shrinking cross-sectional area of the specimen. Strain softening exacerbates the localization phenomenon by causing adjacent areas to elastically unload. As the rate and magnitude of strain softening decreases, the neck becomes more diffuse and stabilizes at a lower axial strain.

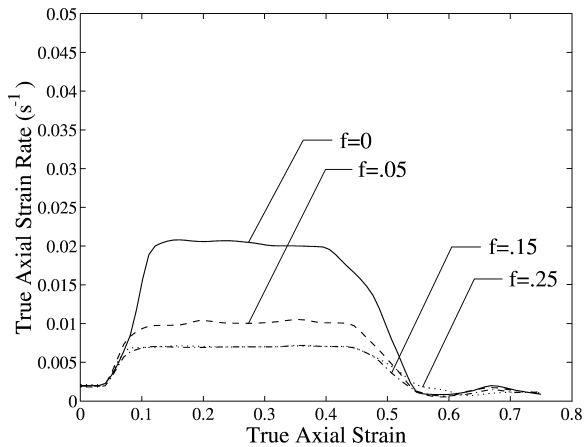

Fig. 32. Uniaxial tension of neat and rubber-modified PC. True axial strain rate, $\dot{\bar{E}}_{yy}$, vs. true axial strain, $\bar{E}_{yy}$.

Table 2
Yield stress and elastic properties of neat and rubber-filled PC

f	Yield stress (MPa)	Young's modulus, E (MPa)	E_{blend}/E	Poisson's ratio, ν
0	65.8	2280	1.0	0.392
0.05	59.0	2140	0.94	0.397
0.15	50.1	1760	0.77	0.414
0.25	40.2	1430	0.63	0.423

3.5.3. Volumetric behavior

The volumetric strain behavior of neat PC and the three blends is depicted in Fig. 33.

In general, the rubber-modified blends behave very similarly. All three materials exhibit less dilatation—both in the elastic and plastic regimes—than neat PC. The lack of volume change is a clear indication that the rubber particles do not cavitate. As f increases, consistent with the decrease in Poisson's ratio, the initial slopes of the curves, dE_{kk}/dE_{yy}, decrease and the curves roll over at lower axial strains. Well predicted by the Mori-Tanaka model in Section 3.5.2, the slight decrease in slope with increasing f in the elastic regime is simply due to the volume averaging of the elastic behavior of the two constituent materials. The roll-over at lower axial strains corresponds to the decrease in yield strain with increasing f observed in the stress–strain behavior in Fig. 31. After yielding, the blend with $f = 0.05$ shows, presumably due to elastic unloading, a drop in

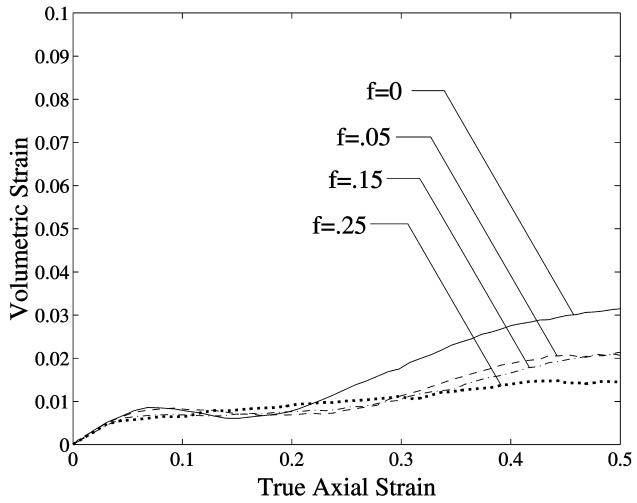

Fig. 33. Uniaxial tension of neat and rubber-modified PC. Volumetric strain, E_{kk}, vs. true axial strain, E_{yy}.

volumetric strain similar to that of the homopolymer but smaller and more elongated. In the blends with $f = 0.15$ and $f = 0.25$, there is no discernable decrease in volumetric strain. This trend agrees with the reduction in magnitude and slope of post-yield strain softening with increasing f observed in Fig. 31.

4. Discussion

Digital image correlation and the associated data reduction schemes developed in this study proved to be powerful tools for the measurement of the large-strain behavior of an inhomogeneously deforming glassy polymer. Showing excellent agreement with simulation results, they successfully measured tensile true stress–strain behavior, full-field strain contours, and volumetric strain.

Tensile true stress–strain behavior is the most fundamental mechanical property of a material, but it is largely unavailable for polymers that neck and draw in the manner of PC. The ability to obtain reliable data for these types of materials will be of great assistance in the development of constitutive models.

Experimental full-field strain contours provide invaluable information about deformation mechanisms. As illustrated in Section 3.5.1, they quantify not only the degree of localization but also the modes of deformation—shearing and/or axial stretching. This information has important implications, particularly for the toughening of polymers. The primary way to toughen polymers is to increase the volume of material involved in the deformation process prior to fracture. Full-field strain contours of notched bend tests, for example, would provide a quantitative measure of the deformation fields in the vicinity of the notch.

Volumetric strain is a quantity critical for the complete understanding of polymer behavior. In homopolymers, it is an indicator of cavitation and/or crazing and, in semi-crystalline homopolymers, crystal fragmentation. In filled polymers, it is also a sign of particle cavitation or debonding. In this study, the small volume change exhibited by the rubber-filled materials indicates that the rubber particles do not cavitate under the low triaxiality conditions of uniaxial tension.

The technique shows great promise, and what shortcomings it does possess could be readily overcome. Strictly constant strain rate true stress–strain behavior could be calculated by constructing composite macroscopic true stress–strain curves from tests performed at applied strain rates an order of magnitude apart. The uncertainty arising from combining strain data from two separate tests at two different orientations in order to calculate volumetric strain could be eliminated by adding a second camera or other optical device to capture the strains in the third dimension simultaneously.

Acknowledgements

This research was funded through the MIT Center for Materials Science and Engineering, NSF MRSEC Grant No. DMR-98-08941, and the AFOSR DURINT on Microstructure, Processing and Mechanical Performance of Polymeric Nanocomposites, Grant No. F49620-01-1-0447.

We would like to thank Correlated Solutions (West Columbia, SC) for providing custom software and a pre-release version of their commercial product, ‘Vic-2D’. Product details and contact information can be found at the CSI website, www.correlatedsolutions.com. We are also grateful to Bayer Corporation, Pittsburgh, PA, for supplying the material used in the study.

Appendix A. Finite element model of uniaxial tension test

Since shear banding occurs during the uniaxial tension test, the entire specimen, including the grip sections, was modeled with 2400 elements of ABAQUS type C3D20. The mesh is shown in Fig. 34(a), and the boundary conditions are illustrated in Fig. 34(b).

An Instron 5582 load frame with self-aligning manual grips was used in the experiments. With this set-up, the bottom grip is fixed while the top grip is free to rotate about a double pin joint 32 cm above the top grip. In the simulation, therefore, the boundary conditions on the 3-faces of the bottom grip were such that all but the upper-most two rows of nodes were fixed in all three directions. All three degrees of freedom on all but the bottom-most two rows of nodes on the 3-faces of the top grip were tied to a single node at the center of the top grip. A rigid beam element of type

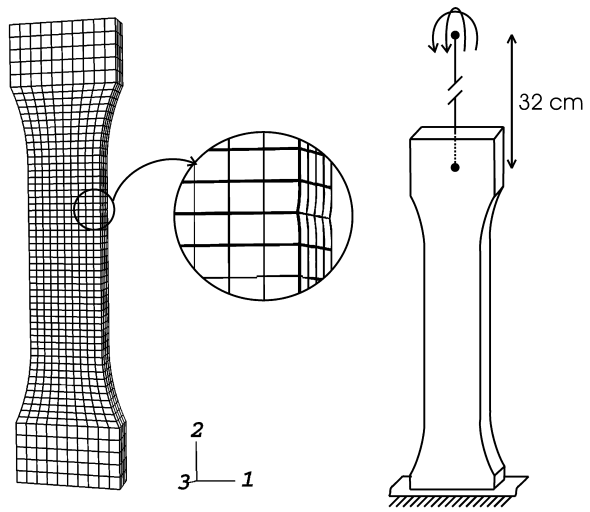

Fig. 34. (a) Tensile bar finite element mesh with close-up of defect, (b) finite element model boundary conditions.

CONN3D2 was defined between that node and a node 32 cm away in the 2-direction. The top, or driver node, was fixed in the 1-direction and 3-direction. The driver node was displaced at a constant rate of 0.095 mm/s in the 2-direction. The macroscopic load, P, was obtained from the reaction force in the 2-direction at the driver node.

Appendix B. Predicting effective blend moduli

The theory of Mori and Tanaka [14] has been widely used to calculate the effective properties of composites. For the case of spherical elastic inclusions in an elastic matrix, the bulk and shear moduli, as expressed by Wang et al. [16], are respectively given by

$$\kappa_{\text{blend}} = \kappa_{\text{m}} + f\frac{\kappa_{\text{m}}(\kappa_{\text{p}} - \kappa_{\text{m}})}{(1-f)\alpha(\kappa_{\text{p}} - \kappa_{\text{m}}) + \kappa_{\text{m}}} \tag{20}$$

and

$$\mu_{\text{blend}} = \mu_{\text{m}} + f\frac{\mu_{\text{m}}(\mu_{\text{p}} - \mu_{\text{m}})}{(1-f)\beta(\mu_{\text{p}} - \mu_{\text{m}}) + \mu_{\text{m}}}, \tag{21}$$

where subscripts ‘m’ and ‘p’ denote properties of the matrix and particle, respectively. The parameters α and β are given by

$$\alpha = \frac{1}{3}\left(\frac{1+\nu}{1-\nu}\right) \tag{22}$$

and

$$\beta = \frac{2}{15}\left(\frac{4-5\nu}{1-\nu}\right), \tag{23}$$

where ν is the Poisson’s ratio of the matrix. κ_{m} and μ_{m} are calculated as 3520 and 819 MPa, respectively, from the properties in Table 2 and the theory of elasticity. κ_{p} is taken as 2000 MPa and, since $\mu_{\text{p}} \ll \mu_{\text{m}}$, Eq. (22) can be simplified to

$$\mu_{\text{blend}} = \mu_{\text{m}}\left(1 - \frac{f}{1-\beta(1-f)}\right). \tag{24}$$

The Poisson’s ratio and tensile modulus of the blend, E_{blend}, are calculated from Eqs. (20) and (24) and the theory of elasticity.

References

[1] Buisson G, Ravi-Chandar K. Polymer 1989;31:2071–6.
[2] G’Sell C, Hiver JM, Dahoun A, Souahi A. J Mater Sci 1992;27:5031–9.
[3] Nazarenko S, Bensason S, Hiltner A, Baer E. Polymer 1994;35:3883–91.
[4] Haynes AR, Coates PD. J Mater Sci 1996;31:1843–55.
[5] Gloaguen JM, Lefebvre JM. Polymer 2001;42:5841–7.
[6] G’Sell C, Hiver JM, Dahoun A. Int J Solid Struct 2002;39:3857–72.
[7] Laraba-Abbes F, Ienny P, Piques R. Polymer 2003;35:3883–91.
[8] Johnson MD. Master’s Thesis, Massachusetts Institute of Technology, Cambridge, MA; 2001.
[9] Bailey HH, Blackwell FW, Lowery CL, Ratkovic JA. USAF Rand Report R-2057/1-PR; 1976.
[10] Schreier HW, Braasch JR, Sutton MA. Opt Engng 2000;39:2915–21.
[11] Schreier HW, Sutton MA. Exp Mech 2002;42:303–10.
[12] Boyce MC, Parks DM, Argon AS. Mech Mater 1988;7:15–33.
[13] Arruda EM, Boyce MC. Int J Plast 1993;9:697–720.
[14] Mori T, Tanaka K. Acta Metal 1973;21:571–4.
[15] Danielsson M, Parks DM, Boyce MC. J Mech Phys Solids 2002;50:351–79.
[16] Wang X, Xiao K, Ye L, Mai Y, Wang CH, Francis Rose LR. Acta Mater 2000;48:579–86.